

AperTO - Archivio Istituzionale Open Access dell'Università di Torino

Core-Shell Structure of Palladium Hydride Nanoparticles Revealed by Combined X-ray Absorption Spectroscopy and X-ray Diffraction

This is the author's manuscript

Original Citation:

Availability:

This version is available <http://hdl.handle.net/2318/1658455> since 2018-01-20T19:25:23Z

Published version:

DOI:10.1021/acs.jpcc.7b04152

Terms of use:

Open Access

Anyone can freely access the full text of works made available as "Open Access". Works made available under a Creative Commons license can be used according to the terms and conditions of said license. Use of all other works requires consent of the right holder (author or publisher) if not exempted from copyright protection by the applicable law.

(Article begins on next page)

This is the author's final version of the contribution published as:

Bugaev, A. L.; Guda, A. A.; Lomachenko, K. A.; Shapovalov, V. V.; Lazzarini, A.; Vitillo, J. G.; Bugaev, L. A.; Groppo, E.; Pellegrini, R.; Soldatov, A. V.; van Bokhoven, J. A.; Lamberti, C.

Core-Shell Structure of Palladium Hydride Nanoparticles Revealed by Combined X-ray Absorption Spectroscopy and X-ray Diffraction.

J. Phys. Chem. C **2017**, *121*, 18202-18213.

Doi: 10.1021/acs.jpcc.7b04152

The publisher's version is available at:

<http://pubs.acs.org/doi/10.1021/acs.jpcc.7b04152>

When citing, please refer to the published version.

Link to this full text:

[inserire l'handle completa, preceduta da <http://hdl.handle.net/>]

This full text was downloaded from iris-AperTO: <https://iris.unito.it/>

Core-Shell Structure of Palladium Hydride Nanoparticles Revealed by Combined X-ray Absorption Spectroscopy and X-ray Diffraction

Aram L. Bugaev^{*,†,‡}, Alexander A. Guda[†], Kirill A. Lomachenko^{†,§}, Viktor V. Shapovalov[†], Andrea Lazzarini^{‡,||}, Jenny G. Vitillo[‡], Lusegen A. Bugaev[†], Elena Groppo[‡], Riccardo Pellegrini[⊥], Alexander V. Soldatov[†], Jeroen A. van Bokhoven[#], Carlo Lamberti^{†,‡}

[†]Smart Materials International Research Center, Southern Federal University, Sladkova 174/28, 344090 Rostov-on-Don, Russia. E-mail abugaev@sfedu.ru

[‡]Department of Chemistry, NIS and CrisDi Interdepartmental Centres, asn INST reference center, University of Turin, Via P. Giuria 7, 10125 Turin, Italy; carlo.lamberti@unito.it

[§]European Synchrotron Radiation Facility, 71 avenue des Martyrs, 38043 Grenoble, France

^{||}inGAP Centre for Research Based Innovation, Department of Chemistry, University of Oslo, P.O. Box 1033, N-0315 Oslo, Norway

[⊥]Chimet SpA - Catalyst Division, Via di Pesciola 74, 52041 Vicinaggio Arezzo, Italy

[#]Institute for Chemical and Bioengineering, ETH Zurich, Vladimir-Prelog-Weg 1, 8093 Zurich, Switzerland and Laboratory for Catalysis and Sustainable Chemistry, Paul Scherrer Institute, 5232 Villigen, Switzerland

ABSTRACT

We report an in situ, temperature and H₂ pressure-dependent, characterization of (2.6 ± 0.4) nm palladium nanoparticles supported on active carbon during the process of hydride phase formation. For the first time the core-shell structure is highlighted in the single-component particles on the basis of a different atomic structure and electronic configurations in the inner “core” and surface “shell” regions. The atomic structure of these particles is examined by combined X-ray powder diffraction (XRPD), which is sensitive to the crystalline core region of the nanoparticles, and by first shell analysis of extended X-ray absorption fine structure (EXAFS) spectra, which reflects the averaged structure of both the core and the more disordered shell. In whole temperature range (0–85 °C), XRPD the analysis confirms the existence of two well-separated α- and β- hydride phases with the characteristic flat plateau in the phase transition region of the pressure-lattice parameter isotherms. In contrast, first shell interatomic distances obtained from EXAFS exhibit a smoother behavior in the phase transition region, typical for nanostructured palladium. Such difference is explained by distinct properties of bulk “core” which has crystalline structure and sharp phase transition, and surface “shell” which is amorphous and absorbs hydrogen gradually without forming distinguishable α- and β- phases. Combining EXAFS and XRPD we extract, for the first time, the Pd-Pd first-shell distance in the amorphous shell of the nanoparticle, that is significantly shorter than in the bulk core and relevant in catalysis. The core/shell model is supported by the EXAFS analysis of the higher shells, in the frame of the multiple scattering theory, showing that the evolution of the third shell distance ($\Delta R_3/R_3$) is comparable to the evolution of ($\Delta a/a$) obtained from XRPD since amorphous PdH_x shell gives a negligible contribution in this range of distances. This operando structural information is relevant for the understanding of structure-sensitive reactions. Additionally, we demonstrate the differences in the evolution of the thermal parameters obtained from EXAFS and XRPD along the hydride phase formation.

1. Introduction

Palladium-based nanomaterials are extensively used as catalysts,¹⁻¹⁷ sensors,^{18, 19} bio-sensors,²⁰⁻²⁴ and in electrochemistry.^{21, 25} In a number of industrial applications, supported palladium nanoparticles are used to catalyze hydrogenation reactions.²⁶⁻³⁴ In the presence of hydrogen, they form different types of hydrides,³⁵⁻⁴⁸ whose relative abundance affects the catalytic performances, especially in terms of selectivity.^{31, 49, 50} Therefore, understanding the structure of palladium hydride phases and building an atomistic model of hydride phase formation in palladium nanoparticles is a problem of high scientific interest and industrial relevance.

Bulk palladium exhibits two hydride phases depending on the stoichiometric atomic ratio x of the PdH_x .⁵¹ The region $0 < x \leq 0.03$ corresponds to the α -phase, while in the region of $x \geq 0.58$ the β -phase is formed. The coexistence of these phases is observed in the region from 0.03 to 0.58. Formation of the hydride phase does not change the symmetry of the initial face centered cubic lattice of the palladium bulk, but leads to an increase of the cell parameter. The latter has a stepwise behavior at the concentrations corresponding to the formation of α - and β - phases, while within each of the phases it linearly increases with x . Palladium nanoparticles are expected to show different thermodynamics of hydrogen absorption in comparison to bulk materials due to a considerable contribution of the surface.^{40, 52} Phase separation was also observed in palladium particles down to nanometer size,^{53, 54} but the relationship between H_2 equilibrium pressure (P_{H_2}) and x loading differs from bulk and strongly depend on the size and shape of the nanoparticles.³⁹ This affects that the maximum x loading of hydrogen in the β -phase, and the extension of the plateau between α - and β -phases.

In the present work, we focus on the process of hydride phase formation in carbon-supported palladium nanoparticles (average particle size of 2.6 nm, with 0.4 nm in standard deviation) as a function of temperature (0 - 85 °C) and P_{H_2} (0 - 1000 mbar), by coupling simultaneous X-ray powder diffraction (XRPD) and extended X-ray absorption fine structure spectroscopy (EXAFS) experiments with independent volumetric measurements. XRPD allows monitoring the increase of the cell parameter a during the hydride formation, differentiating between the α - and β - hydride phases, but it is scarcely informative for nanoparticles with size below 1 nm^{53, 54} (that do not contribute to the Bragg reflections) and to the external shell of nanoparticles (because of disorder effects intrinsic of surface layers). Being element specific, EXAFS selectively probes the local environment around the Pd absorbing atom, yielding average Pd-Pd interatomic distances, coordination numbers and Debye-Waller parameters, and providing important complementary information on the surface of the nanoparticles,⁵⁵⁻⁶⁷ that is merged with the information on the core. Finally, volumetric measurements^{68, 69} provide quantitative information on the amount of hydrogen absorbed in terms of average H/Pd atomic ratio, provided that the hydrogen uptake from the support is properly taken into account.

The synergic coupling of the three techniques highlighted clear differences in the structural and electronic configuration of the palladium atoms in the shell and in the core of the nanoparticles during the $\text{Pd} \leftrightarrow \text{PdH}_x$ phase transition. Particularly, XRPD revealed the subsequent formation of two well-separated α - and β - hydride phases with a flat plateau, similar to that obtained for bulk Pd. In contrast, the contribution of the surface to the first shell EXAFS analysis⁷⁰ resulted in a smoother evolution of the Pd-Pd first shell interatomic distance, which evidences the presence of a core-shell structure in the PdH_x nanoparticles. Unlike the previously reported independent XRPD and first shell EXAFS study,⁷¹ performed on similar sized Pd nanoparticles (2.5 ± 0.5 nm) and reporting only the starting (Pd) and final ($\text{PdH}_{0.4}$) points of the of the PdH_x system at ambient temperature, we collected more than hundred points in the P_{H_2} -temperature plane by simultaneous XRPD and EXAFS data collection (the latter analyzed till the fourth shell), which was a crucial step to highlight the core-shell structure. We have also observed a different behavior of the Debye-Waller parameter in EXAFS and isotropic

atomic displacement in XRPD fits, which is explained by the fundamental difference of the two methods.

2. Materials, Experiments and Methods

2.1. Sample preparation and characterization.

5 wt.% Pd on carbon catalyst supplied by Chimet S.p.A. has been prepared by deposition-precipitation method⁷² on activated carbon of wood origin (surface area = 980 m²g⁻¹; pore volume = 0.62 cm³g⁻¹).^{73, 74} Palladium black sample has been prepared following a procedure similar to that adopted for the catalyst preparation, but omitting the support, and successively reduced in H₂ at 120 °C, resulting in a stable bulk Pd⁰ phase.

2.2. In situ X-ray absorption spectroscopy and X-ray powder diffraction setup

Pd K-edge X-ray absorption spectroscopy and X-ray powder diffraction data were collected at the BM01B^{75, 76} (Swiss-Norwegian Beamline, successively moved to the BM31 port) of the European Synchrotron Radiation Facility (ESRF), Grenoble, France. The beamline allows a rapid (about 30 s) plug and play switch between X-ray absorption and X-ray diffraction setups, allowing to measure for each of the selected P_{H_2} -temperature conditions, both EXAFS and XRPD on exactly the same point of the PdH_x phase diagram. A boron glass capillary 1.0 mm in diameter filled with the sample powder was connected to a remotely controlled gas rig enabling to vary the P_{H_2} during the experiment. Vacuum pump was connected to the system for outgassing, providing a minimal pressure lower than 0.1 mbar. Nitrogen-based gas blower positioned above the sample allowed to control the temperature from values below 0 °C and up to 150 °C. To remove the surface oxide layer formed on the palladium nanoparticles exposed to air,⁷⁷ initial pretreatment of the sample was performed at 125 °C in 200 mbar of hydrogen for 30 minutes. EXAFS/XRPD data were collected at five different temperatures from 0 to 85 °C increasing the pressure from 0 to 1000 mbar. Since the temperatures of the gas blower set-point may differ from the real temperature of the catalyst, we report the temperatures of the samples. These temperatures were obtained by matching the pressures of the phase transition to the corresponding point of the Van 't Hoff plot, derived from the volumetric measurements of this sample (see Section 2.3 below, Section S4 and Figure S10 of the ESI). The pressure always corresponds to the absolute hydrogen pressure, which was the only gas used. The pressure steps were chosen in the way to have more experimental points in the region of α - to β - phase transition. To completely remove the hydrogen loaded in the sample during the previous isotherm, the sample was outgassed for 30 minutes at 125 °C before each measurement.

X-ray absorption spectra at Pd K-edge were obtained in the transmission mode by continuous scanning of the double crystal Si(111) monochromator from 24.1 to 25.4 keV taking 5 minutes per spectrum. Palladium foil was measured simultaneously with each spectrum for energy calibration using a third ionization chamber. Palladium black powder was used as a reference sample. X-ray powder diffraction was measured using 0.50544(2) Å radiation, selected by a Si(111) channel-cut monochromator. CMOS-Dexela 2D detector positioned at the distance of 250.24(7) mm from the sample resulted in a 2θ range from 2 to 52 degrees ($d_{\min} = 0.58$ Å). The values of the photon wavelength, sample to detector distance and detectors tilts have been optimized by Rietveld refinement of NIST LaB₆ and Si samples and kept fixed in the refinement of the Pd/C samples. For better statistics 20 diffraction images and 20 dark images (without X-ray beam) with acquisition time of 1 second were collected at each experimental point.

X-ray absorption spectra were analyzed in Demeter 0.9.21 package⁷⁸ including background subtraction, normalization, energy calibration, and single-shell Fourier analysis. A real space data fitting in the R-range from 1.5 to 3.2 Å was performed to the Fourier-transformed k^2 -weighted data in the k -range from 5 to 12 Å⁻¹, corresponding to the number of independent points $2\Delta k\Delta R/\pi > 7$. The low k -region (2 – 5 Å⁻¹) was intentionally excluded from the analysis to minimize the Pd-C

contribution from interaction of the nanoparticles with the support. The fit included four parameters: the first shell Pd-Pd interatomic distance (R_1), the Debye-Waller factor (σ^2), energy shift (ΔE_0) and coordination number (N). The parameters ΔE_0 and N were considered as common variables for all spectra. The value of the passive electron reduction factor $S_0^2 = 0.83 \pm 0.03$ was obtained by fitting the spectrum of palladium foil and kept constant in the optimization of all the spectra collected on the Pd-catalyst. For higher-shell analysis (Section 4.3) the R -range from 1.2 to 5.5 Å and k -range from 3.0 to 14.0 Å⁻¹ were used ($2\Delta k\Delta R/\pi > 30$). In the fits S_0^2 was fixed to 0.83 and a single ΔE_0 was optimized for all single scattering (SS) and multiple scattering paths; four independent R_1, R_2, R_3, R_4 , distances were optimized for the four SS paths, with four independent (σ_i^2) parameters, resulting in 9 independent parameters. The coordination numbers of the first four shells in the nanoparticles have been fixed to the size-dependent values given by the model developed by Calvin et al.⁷⁹, see below Eq. (3). To minimize the number of optimized parameters, guaranteeing stability to the fits, for all relevant MS paths, the path length and the corresponding σ^2 parameter were constrained by the values of R_i and σ_i^2 as already successfully done in other studies.⁸⁰⁻⁸² For both first shell and higher shells analyses, the fitting was performed in R -space using theoretical amplitudes and phases calculated by FEFF6 code.⁸³

2D XRPD patterns were processed by PyFAI⁸⁴ software which executes fast averaging, background subtraction and integrating of images to obtain $I(2\theta)$ patterns. Rietveld refinement was performed in Jana2006 code.⁸⁵ Profile parameters were optimized by fitting the diffraction patterns of bare and the most hydrogenated samples at each temperature. In the final refinement, we optimized of the fractions of α and β phases and the cell parameters corresponding to each phase.

2.3. Volumetric measurements

Hydrogen sorption isotherms were measured on a commercial volumetric apparatus (*Micromeritics ASAP2020*). The instrument was equipped with 4 pressure transducers, allowing to investigate the sorption process at very low equilibrium pressures (down to 10⁻⁴ mbar). Prior to the measurements, the Pd/C powders (1.4 g) were activated on a vacuum line equipped with a turbomolecular pump ($P < 10^{-4}$ mbar): after degassing at 120 °C for 3 h, the sample was subjected to two H₂ absorption/desorption cycles at 120 °C in hydrogen (absorption pressure: ~100 mbar, desorption pressure: dynamic vacuum) to guarantee a full reduction of the palladium nanoparticles. Then the sample was exposed to 100 mbar of H₂ and cooled down to room temperature. The sample was successively transferred inside a glove box (M Braun Lab Star Glove Box supplied with pure 5.5 grade N₂, < 0.5 ppm O₂, < 0.5 ppm H₂O) before being inserted into the measurement cell and degassed at room temperature for 1 h on the volumetric apparatus. The H₂ uptake of the (Pd-free) carbon support was measured in the same conditions adopted for the Pd/C catalyst, after activation in dynamic vacuum at 120°C overnight. Hydrogen gas (99.9999 vol% purity) was supplied by Rivoira SpA. The isotherms reported in the following for the Pd/C systems were obtained from the measured ones after the subtraction of the H₂ uptake measured in the same conditions for the activated carbon support.

3. Results

The narrow particle size distribution of the nanoparticles is a fundamental prerequisite for extracting reliable information from both XRPD and EXAFS data. Therefore, the Pd/C catalyst was initially investigated by means of high resolution transmission electron microscope (HRTEM: JEOL 3010-UHR instrument operating at 300 kV and equipped with a 2k × 2k pixels Gatan US1000 CCD camera), to determine in a direct way the average particle size and the particle size distribution. A representative TEM micrograph is reported in Figure 1, where the palladium particles appear homogeneously distributed on the carbon support in an isolated form without aggregates. A careful

analysis of several TEM images containing more than 500 independent particles revealed that the average size of the palladium particles is 2.6 ± 0.4 nm.

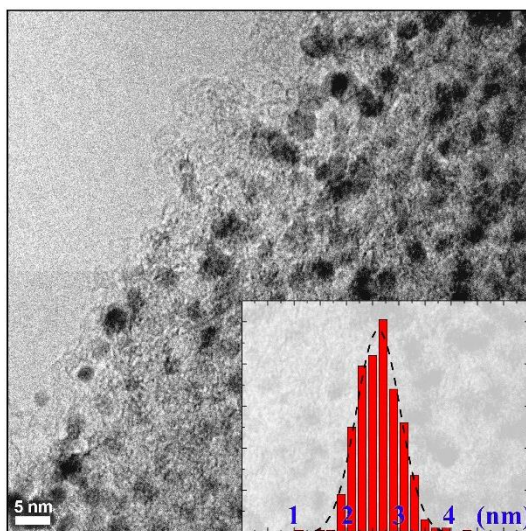


Figure 1. Representative TEM micrograph of the Pd/C sample and corresponding particle size distribution.

In a second step, the formation of the palladium hydride phase as a function of the hydrogen pressure and temperature was investigated by coupling synchrotron EXAFS and XRPD experiments (Figure 2) with volumetric measurements (see Sections S2-S4 of the ESI for details in the data collection), obtained almost simultaneously. The progressive formation of the Pd-hydride phase upon increasing P_{H_2} at constant temperature leads to the expansion of the palladium lattice (i.e. the increase of the first shell Pd-Pd interatomic distance), because of the insertion of hydrogen in the octahedral interstitial positions. The increase of the first shell Pd-Pd interatomic distances is observed in the Fourier-transforms of the Pd K-edge EXAFS spectra (Figure 2a) and leads to a shift of the XRPD reflections towards smaller 2θ angles (Figure 2b).

The whole set of EXAFS data shown in Figure 2a was analyzed with a first-shell Fourier approach (Section S2). The Pd-Pd distance was found to change along each isotherm as a function of P_{H_2} . The resulting palladium hydride pressure-distance curves are shown in Figure 3a. It is worth noticing that the lattice expansion process is accompanied by an increase in the Debye-Waller parameter, σ^2 , which will be discussed in Section 4.4.

In contrast to EXAFS, XRPD is a phase-specific technique. Hence, it enables to analyze separately the α - and β - hydride phases present in the sample at each point of the isotherm. The relative concentrations of the α - and β - phases and the cell parameters within each phase have been determined by a 2-phases Rietveld refinement procedure (see Section S3 of the ESI). To plot the structural isotherms obtained from XRPD in a way directly comparable with the EXAFS data (Figure 3a), we calculated the averaged cell parameter as a weighted sum

$$a = (1 - n) \cdot a_{\alpha} + n \cdot a_{\beta}, \quad (1)$$

where a_{α} and a_{β} are the refined lattice parameters of the α - and β - phases respectively, and n the refined fraction of the β -phase. The evolution of the cell parameter as a function of P_{H_2} at different temperature is plotted in Figure 3b.

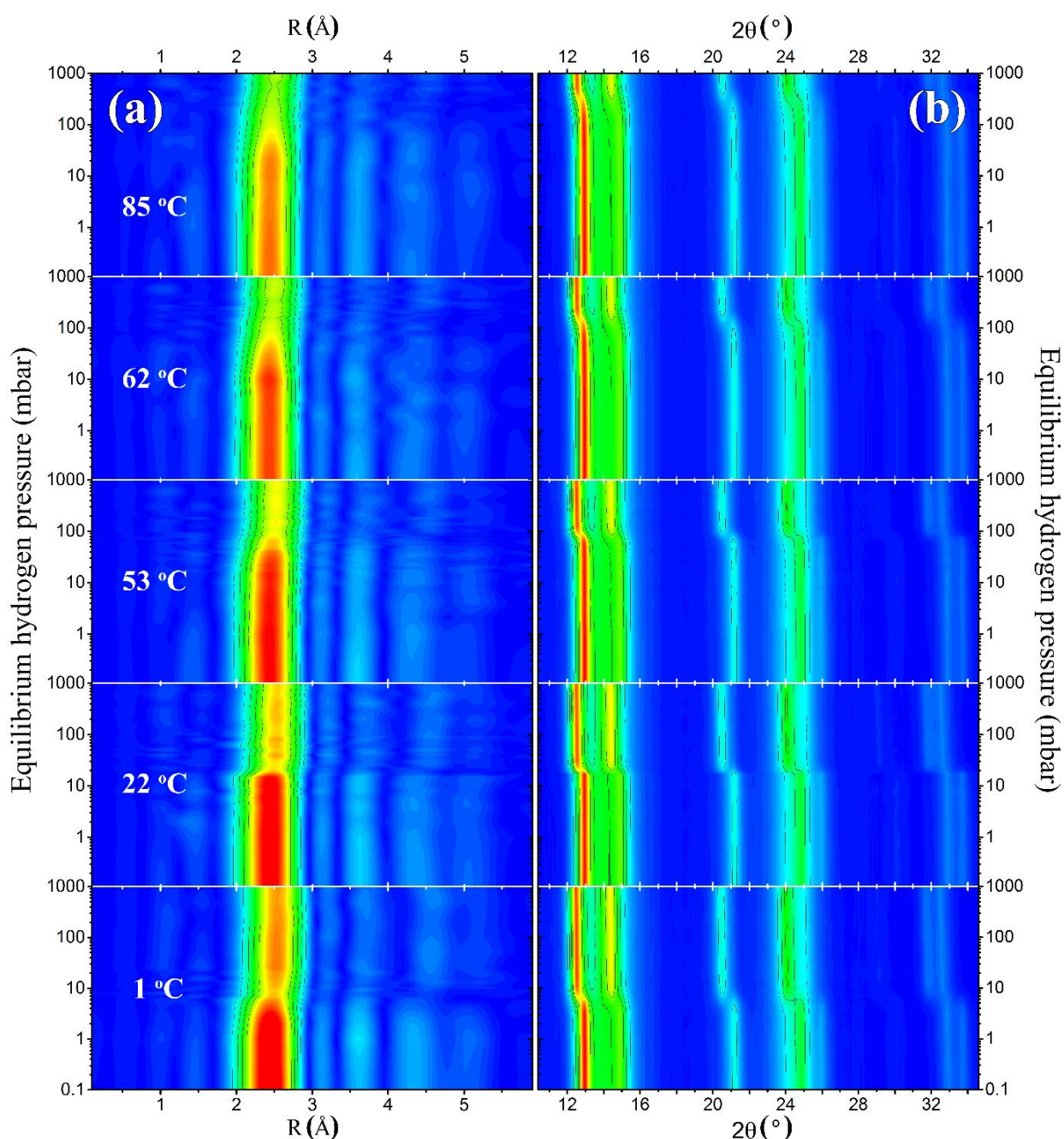


Figure 2. Evolution of the k^2 -weighted, phase uncorrected Fourier-transformed EXAFS data $|\chi(R)|$ (part a), and XRPD patterns (part b) during the palladium hydride formation at different temperatures. For all FT-EXAFS spectra the same color scale has been adopted, which allows to appreciate the intensity reduction of the first shell Pd-Pd contribution (2-3 Å range) due to structural (PdH_x formation) and thermal disorder. Each XRPD pattern has been normalized to its total scattering area.

Similar sequences were collected through independent volumetric measurements resulting in the pressure-composition isotherms reported in Figure 3c, that give information on the stoichiometric H/Pd ratio (x) at the given P_{H_2} and temperature.

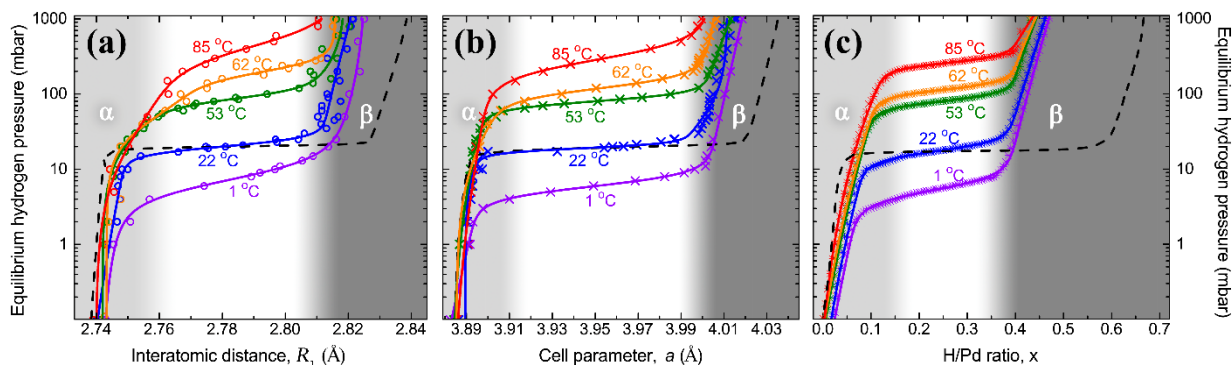


Figure 3. Pressure- R_1 , pressure- a and pressure- x isotherms obtained from EXAFS (a), XRPD (b), and volumetric technique (c) for Pd/C at different temperatures (colored scatters) and palladium bulk (Pd-black) at 22 °C (black dashed line). Solid colored lines correspond to the best fits by a model double-exponential function. The abscissa of part (b) is the averaged cell parameter defined in Eq. (1). Light gray, white and dark gray regions define qualitatively pure α -, mixed-, and pure β - phases, respectively, for the Pd/C sample.

4. Discussion

4.1. The PdH_x phase diagram for Pd/C

The pressure-structure isotherms shown in Figure 3ab are very similar to the pressure-composition curves obtained from volumetric measurements (Figure 3c), which give information on the H/Pd ratio at a given temperature and pressure. All the diagrams are characterized by three distinct regions: (i) a pre-plateau region, relative to the formation of the α -phase (light gray region); (ii) the plateau, corresponding to the phase transition from the solid solution to the β -phase (white region); (iii) a post-plateau region, where the solid solution of hydrogen in the metal hydride is formed (dark gray region).⁸⁶ As widely reported for bulk palladium, the pressure corresponding to the plateau increases with the temperature, and at the same time the miscibility gap of the solid solution with the hydride phase decreases.^{38, 40, 86-94}

As a consequence of the nanometric size,^{36, 71, 86, 95} for palladium nanoparticles the hydrogen-uptake and the lattice parameters at the end of each plateau is lower than that for bulk palladium at similar temperatures, e.g. at 22 °C only $\text{PdH}_{0.4}$ was obtained in Pd/C vs $\text{PdH}_{0.6}$ for palladium black. In contrast, the thermodynamic of hydrogen absorption seems not to be influenced by the nanometric size of the palladium particles. Indeed, the enthalpic and entropic values obtained from the Van 't Hoff plot reported in Figure S10 ($\Delta H = -36.9 \pm 3.7 \text{ kJ} \cdot \text{mol}_{\text{H}_2}^{-1}$; $\Delta S = 92.0 \pm 9.2 \text{ J} \cdot \text{K}^{-1} \cdot \text{mol}_{\text{H}_2}^{-1}$) are close to those reported in the literature for bulk palladium ($\Delta H = -37.2 \text{ kJ} \cdot \text{mol}_{\text{H}_2}^{-1}$; $\Delta S = 92.5 \text{ J} \cdot \text{K}^{-1} \cdot \text{mol}_{\text{H}_2}^{-1}$),⁴⁵ and in agreement with the values reported in the literature for nanometric palladium particles.^{35, 36, 40, 45, 46, 53, 90, 93, 96-98} The absence of a clear dependence of the entropic/enthalpic terms on the palladium particle size and shape has been previously reported,^{35, 45, 46} and explained in terms of an enthalpy-entropy compensation effect in H-absorption in both palladium bulk and nanoparticles.⁴⁵

4.2. Evolution of the Pd-Pd distances in the core and shell of the PdH_x nanoparticles

As a general tendency, the palladium nanoparticles undergo a less sharp phase transition than bulk palladium, which was explained in the literature by size and shape dispersion phenomena.⁹⁶ This effect is evident when comparing the structural and compositional isotherms obtained at 22 °C for Pd/C (blue scatters in Figure 3) and palladium black (dashed line in Figure 3). However, the first shell EXAFS data themselves (Figure 3a) exhibit a less defined plateau than the corresponding XRPD data (Figure 3b). The plateau of the isotherms obtained by EXAFS are spanned in a wider pressure range with respect to the same plateau observed by XRPD at all the investigated temperatures. This

discrepancy is absent for palladium black, suggesting that it is a characteristic feature of the sample, and not of the method.

The systematic difference in the behavior of the first shell EXAFS and XRPD data can be better appreciated by plotting the evolution of the first Pd-Pd distance obtained by EXAFS (R_1) as function of the cell parameter a obtained by XRPD for all the different pressures and temperatures, as shown in Figure 4a. For palladium black, the data can be fitted by a straight line of the type $R_1 = m \times a$ (dashed line in Figure 4a), where the fitted value of $m = 0.71 \pm 0.01$ agrees with that expected from the geometric relationship between the cell parameter and the interatomic distance in a face centered cubic lattice, given by $1/\sqrt{2} = 0.707$. A minor difference between $\sqrt{2}R_1$ and a is originated from systematic error associated to each method (e.g. error in determining sample-to-detector distance in XRPD, calculated phases and correlation between E_0 and R_1 in EXAFS, etc.). To minimize this systematic error, we corrected the a values obtained for the nanoparticles by factor 0.996 determined comparing XRD and EXAFS data obtained on Pd metallic bulk. A larger deviation from this linear law is observed for palladium nanoparticles in Pd/C. In particular, in the regions corresponding to pure α - and β - phases, the first shell R_1 values obtained from EXAFS grow faster than the cell parameter obtained by XRPD, while during the phase transition an opposite behavior is observed. To emphasize this difference, in Figure 4b, the first shell R_1 and a values have been plotted as a function of the H/Pd ratio x determined from the volumetric measurements reported in Figure 3c.

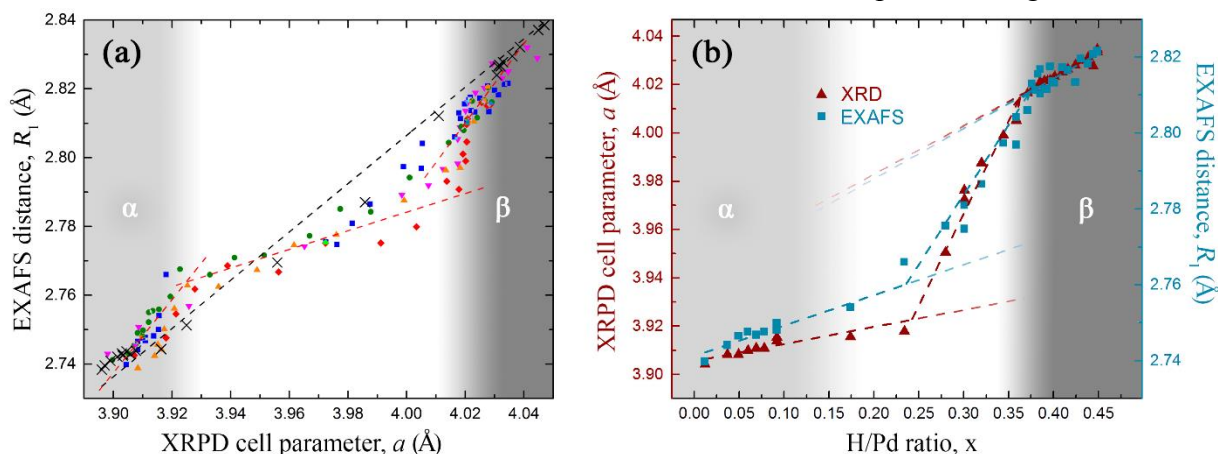


Figure 4. (a) Interatomic first shell distance R_1 obtained from EXAFS vs. cell parameter a obtained from XRPD. The plot contains all the data measured at different temperatures in the pressure range from 0 to 1000 mbar. The different colors of the scatters correspond to different temperatures; the color scheme is kept the same as in Figure 3. Cross scatters refer to palladium black, and the black dashed line is a linear fit of these data. Three red dashed lines emphasize the relation between EXAFS and XRPD for the nanoparticles in the three different regions. (b) Evolution of the XRPD cell parameter (left axis, red triangles) and EXAFS interatomic distances (right axis, blue squares) with the increase of hydrogen loading in the palladium nanoparticles at 22 °C.

The observed discrepancy can be accounted for by considering that the palladium hydride nanoparticles do have a core-shell structure, with a crystalline core that contributes both to the Bragg reflections in the XRPD patterns and to the first shell Pd-Pd distance obtained by EXAFS, and an amorphous shell that contributes only to the latter observable. Similar models of core-shell palladium hydride nanoparticles have been previously discussed, but did not have explicit experimental evidences.^{40, 45, 46, 88, 99, 100} It has also been shown that for nanoparticles with average size of 1 nm, which do not give well-defined Bragg peaks due to the lack of long range order,^{53, 54} the α - β phase separation does not exist and the pressure-composition isotherms lack the plateau region.⁵² A similar behavior should be expected for an amorphous shell of Pd hydride nanoparticle, but cannot be measured directly. Nevertheless, the theoretical $R_1^{shell}(P_{H_2})$ pressure-distance isotherm of the shell can be derived from the available data, by using the XRPD pressure- a isotherm, $a(P_{H_2})$, as

representative of the core, and the EXAFS isotherm, $R_1^{EXAFS}(P_{H_2})$ as the average of the core and shell contributions, according to the following expression:

$$CR_1^{shell}(P_{H_2}) = R_1^{EXAFS}(P_{H_2}) - (1 - C) \frac{1}{\sqrt{2}} a(P_{H_2}), \quad (2)$$

where C is the fraction of atoms located in the amorphous shell. This value was set to 0.6 based on the detailed analysis of EXAFS spectra,⁷⁰ which indicated that the fraction of palladium atoms located in the amorphous surface for Pd nanoparticle of 2.6 nm size is about 60%. In addition, the crystalline size determined from XRPD (full widths of the Bragg peaks) does not change significantly along the hydride phase formation at all studied temperatures, which indicates that the ratio between core and shell can be fixed for all experimental points. The resulted theoretical isotherm (22 °C) for the amorphous shell of the nanoparticle is shown in Figure 5a together with the two experimental curves that have been used to obtain it. As expected, the shell absorbs hydrogen gradually, and the corresponding isotherm does not result in a well-defined phase transition. The similar simulated isotherms, assuming the shell fraction of 50 and 70% is shown in Figure S11.

From the data reported in Figure 5a, it emerges that the R_1 distance is shorter in the amorphous shell than in the bulk core at any investigated P_{H_2} . This difference is small at low P_{H_2} ($\Delta R_1 < 0.005$ Å) and progressively increases with the hydrogen uptake ($\Delta R_1 = 0.014$ Å). The pressure-distance isotherms obtained for the shell of the nanoparticles (Figure 5b) indicate that the shell part absolutely lack the plateau region at high temperatures. This agrees with the observation done on 1 nm Pd particles exhibiting only the amorphous phase.⁵² In addition, figure emphasize the changes in the slope of the isotherms in the mixed phase region which are most strongly observed at high temperatures. The origin of such slope may be due to the fact that the critical temperature, above which no α - and β - phases do not exist, is lower in the shell than in the core. However, within the quality of the data we cannot prove or disprove this hypothesis.

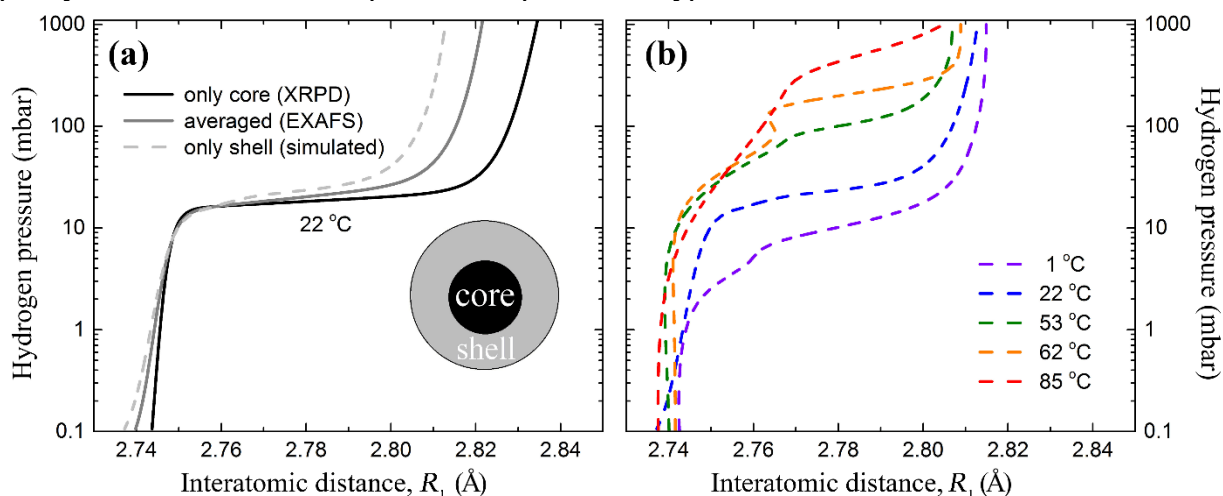


Figure 5. (a) Pressure-distance isotherms of core and shell of the palladium hydride nanoparticle plotted as a function of R_1 . Full curves correspond to the experimental pressure-structure isotherms at 22 °C, as obtained from XRPD data (black) and EXAFS data (dark grey). The dashed line is the theoretical curve, obtained by applying Eq. (2) in the hypothesis of 60% of atoms contributing to the shell ($C = 0.6$, see scheme), and accounts for the behavior of palladium hydrides in the shell of the nanoparticle. (b) Simulated pressure-distance isotherms for the shell part of the nanoparticles at different temperatures. The similar simulated isotherms, assuming the shell fraction of 50 and 70% is shown in Figure S11.

As a final comment, it could be argued that, besides the amorphous shell, ultra-small nanoparticles below 1 nm can also contribute to EXAFS, while escaping from detection by XRPD. However, in the present study, this contribution can be neglected for two reasons: (i) the fraction of particles with diameter below 2 nm is negligible (inset in Figure 1), (ii) there are less atoms inside a 1-nm particle than in the shell of a 2.6 nm particle, which further reduce their effect on the resulting EXAFS

spectrum.^{62, 101} This means that the discrepancies observed between the EXFS and the XRPD data (Figure 4) are actually due to a core-shell effect and not to a size-heterogeneity effect.

4.3. Higher-shell EXAFS analysis

To further confirm the discrepancy between the results obtained from XRPD and first shell EXAFS analyses, and to support our crystalline core / amorphous shell model we report additional higher shell EXAFS analysis on the 22 °C isotherm data for Pd black (Figure 6a) and Pd nanoparticles (Figure 6b). Indeed, higher-shell analysis of EXAFS data provides intermediate-range structural information, being so intermediate between the short range order selectivity of the first shell EXAFS analysis and the long range order typical of XRD technique. To highlight the different behavior of first and higher shells, we have performed EXAFS-analysis in extended R-range from 1.2 to 5.5 Å, using the whole k-range available: 3.0–14.0 Å⁻¹. All contributions with an intensity higher than 0.05 (with respect to the SS first shell Pd-Pd) and with effective path length smaller than 6 Å were taken into account (see Figures S4 and S5). The decrease of coordination numbers in the nanoparticles with respect to the bulk was taken into account using an equation:⁷⁹

$$N_{nano,i} = \left[1 - \frac{3R_i}{2D} + \frac{1}{2} \left(\frac{R_i}{D} \right)^3 \right] N_{bulk,i} \quad (3)$$

where R_i is the effective path length of each path, and D is mean particle size (for the bare nanoparticles, we determined $D = 2.4 \pm 0.8$ nm which is close to the size provided by TEM and XRPD). The so obtained $N_{nano,i}$ values were kept fixed in the fits.

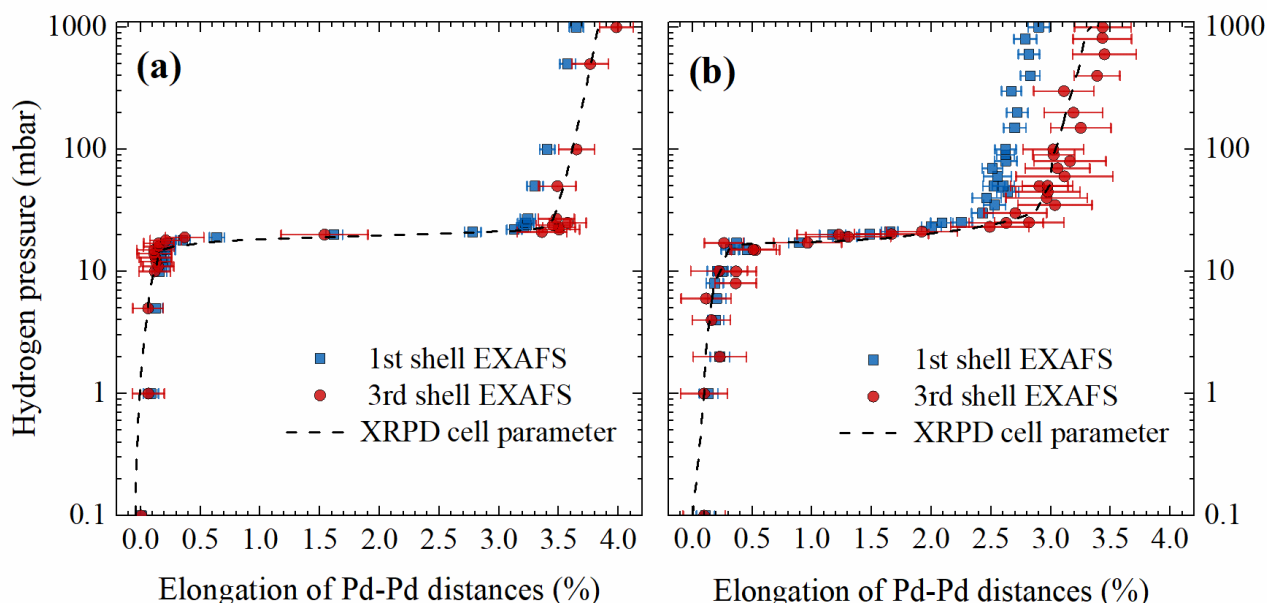


Figure 6. Evolution of the 1st (blue squares) and 3rd (red circles) shells determined by EXAFS for Pd black (a) and Pd nanoparticles (b) during hydride phase formation at 22 °C. The XRPD data is shown as black dashed line.

Figure 6 shows the relative evolution of the interatomic distances for the first and third shells. The figure reports $\Delta R_i/R_{i,0} = (R_i - R_{i,0})/R_{i,0}$ values, being R_i the P_{H_2} -dependent distance of the i -th shell, being $R_{i,0}$ the corresponding value for the pure metallic phase and being $i = 1$ and 3 . The dashed line reports the equivalent $\Delta a/a_0 = (a - a_0)/a_0$ values extracted from XRPD, with obvious meaning. It is clearly seen that for the Pd black sample the same relative elongation is observed for $\Delta R_1/R_{1,0}$, $\Delta R_3/R_{3,0}$, and $\Delta a/a_0$ (Figure 6a). Conversely, in the case of the nanoparticles (Figure 6b), the elongation of the 3rd shell distance is bigger than that of the 1st shell and has a similar behavior as XRPD data. The corresponding $\Delta R_2/R_{2,0}$, $\Delta R_4/R_{4,0}$, curves, referring to the 2nd and 4th shells are not

shown in Figure 6 because their contribution to the oscillatory EXAFS function is much smaller and fully overlapped by the contribution of much stronger MS paths falling in the same R-region (see Figure S4). These facts result in bigger error in their determination.

It is worth underlying that XRPD is still fundamental in giving solidity to our core/shell model because, the error associated to the determination of a by XRPD is much smaller than that related to the determination of R_3 by EXAFS.

4.4. Short and long scale disorder

Both thermal and structural disorder affect both XRPD and EXAFS data, reducing the intensity of the signals at high q or k values, respectively.¹⁰² Consequently, the disorder has been considered in the data analysis, by optimizing the isotropic atomic displacement (U_{iso}) in XRPD and the Debye-Waller parameter (σ^2) in EXAFS. For the data collected at 22 °C, the optimized U_{iso} is about 0.005 Å² for all the patterns in both pure metal and α - and β - hydride phases of the Pd nanoparticles (green squares in Figure 7). Indeed, U_{iso} , describes the oscillation of an atom around its crystallographic position, and is almost insensitive to the crystallographic phase (note that similar U_{iso} values have been obtained for the bulk Pd black phase along the whole isotherm, grey stars). In contrast, the σ^2 obtained from EXAFS analysis is not constant, but increases with P_{H_2} (blue diamonds in Figure 7). For both nanoparticles (blue diamond) and Pd black (black crosses), the σ^2 parameter does not change in the region below 10 mbar, this fact is explained considering that the α -phase contains a very low amount of hydrogen, which does not contribute significantly to the structural disorder. An almost step-wise increase of σ^2 is then observed in the phase transition region around 20 mbar, corresponding to the coexistence of the α - and β - hydride phases, that are characterized by different Pd-Pd interatomic distances. This abrupt change of σ^2 with the hydrogen uptake can be explained by considering that σ^2 reflects the variation in the interatomic distance between the neighboring atoms and includes thermal disorder and static disorder effects.¹⁰³ This effect is even more pronounced for palladium black (black crosses in Figure 7), because the difference in the Pd-Pd interatomic distances in the α - and β - hydride phases is bigger for bulk palladium than for the nanoparticles and because the phase transition occurs in a narrower P_{H_2} interval. Finally, the σ^2 in the pure β -phase does not go back to the starting value due to the significant fraction of hydrogen atoms ($x \approx 0.4$ or 0.6 for nanoparticles or bulk, respectively) incorporated in the interstitial sites of the palladium lattice. Such H atoms create local distortions of the environment of each Pd atoms (that is observed by EXAFS with an increase of σ^2), but since such distortions do not have long range order, they are not detected with diffraction methods. A more detailed discussion on the EXAFS σ^2 parameter increase in the solid solutions can be found in the literature.¹⁰⁴⁻¹⁰⁷

The logical challenge that arises from the discussion reported above, would be to perform the Fourier-analysis of the EXAFS spectra using the separate contributions for the α - and β - phases, as it was done in the XRPD refinement. Indeed, such approach should decrease the values of Debye-Waller parameter in the region of the phase transition. However, in this particular case, such analysis does not give reliable results because there is a strong correlation between $|R_\beta - R_\alpha|$ and σ^2 , where R_α and R_β are the first shell Pd-Pd interatomic distances within each of the phases. This correlation cannot be resolved, because it is limited by the standard resolution of the local structure distortion by EXAFS¹⁰⁸ due to too small value of $|R_\beta - R_\alpha|$ for the measured Δk interval (the Rietveld-refined difference $|R_\beta - R_\alpha|$ in the phase transition region is below 0.07 Å (see Figure S7 of the ESI), while the spatial resolution of our EXAFS data is $\pi/(2k_{\text{max}})^{66} > 0.1$ Å).

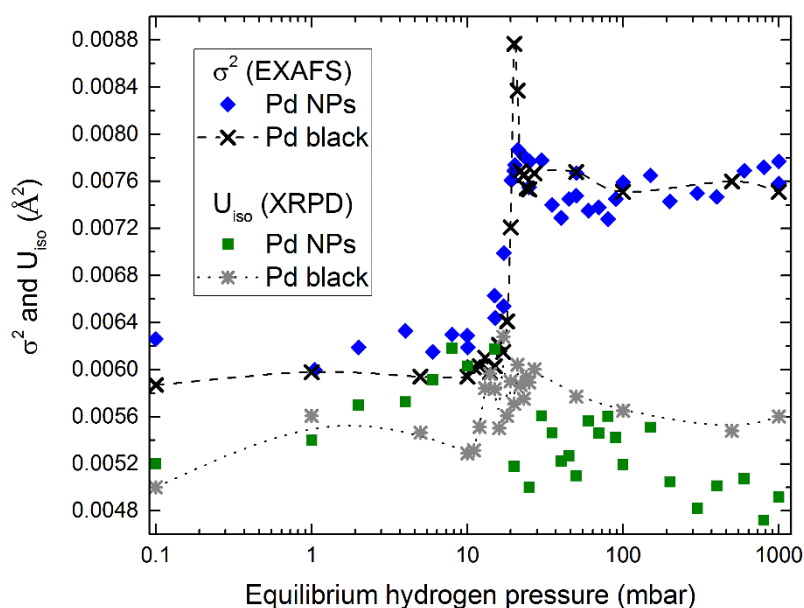


Figure 7. Evolution of the Debye-Waller parameter σ^2 (as determined by EXAFS) for the palladium nanoparticles (blue diamonds) and palladium black (black crosses highlighted by dashed line) upon the hydride phase formation at 22 °C, versus U_{iso} (as determined by XRPD analysis) for the palladium nanoparticles (green squares) and palladium black (grey stars highlighted by dotted line).

5. Conclusions

In this study, we have investigated the process of hydride formation in wide pressure and temperature ranges in carbon-supported Pd nanoparticles having an average size of (2.6 ± 0.4) nm, by coupling volumetric measurements with simultaneous EXAFS and XRPD experiments. The synergic use of the three techniques allowed constructing the PdH_x phase diagram for Pd nanoparticles. During the hydride phase formation, a systematic difference was observed in the evolution of the first shell Pd-Pd interatomic distances as determined by EXAFS and XRPD showing a difference of $\Delta R_1 = 0.014$ Å between core and shell in the β -phase. This difference was shown to be a characteristic feature of the PdH_x nanoparticles. This is the first structural direct evidence of the presence of a core/shell structure in palladium nanoparticles. The crystalline PdH_x core contributes to both XRPD and EXAFS, while the amorphous shell does not contribute to XRPD but is probed by EXAFS. The core exhibits the sharp phase transition and the flat pressure-structure plateau in the isotherms typical of bulk palladium, while the shell exhibits a much smoother behavior. The core/shell model is further supported by the analysis of the evolution of the 3rd shell interatomic distance in the EXAFS data, that exhibits a behavior closer to that observed by XRPD rather than to that of the EXAFS 1st shell.

In addition, we observed for both Pd nanoparticles and bulk palladium samples a different behavior of the σ^2 parameter determined by EXAFS with respect to U_{iso} from XRPD along the hydride phase formation. This difference was explained by the fundamental difference between the long- and short-range disorder contributing to XRPD and EXAFS, respectively. Increased local disorder of the palladium hydride solid solution leads to higher σ^2 in EXAFS, while XRPD shows similar U_{iso} parameter for both dehydrogenated material and hydride phases.

For all the results stated above, the simultaneous *in situ* EXAFS and XRPD data collection was mandatory to highlight the discrepancies between the core and the shell parts of the nanoparticles.

This operando structural information is relevant for structure-sensitive reactions,¹⁰⁹⁻¹¹³ as we have been able, for the first time to determine the actual structure of the active, amorphous catalyst surface.

6. Acknowledgements

ALB, AAG, KAL, VVS, AVS and CL acknowledge Mega-Grant of Ministry of Education and Science of the Russian Federation (14.Y26.31.0001) for funding the research. AAG acknowledges the grant of the President of Russia for young scientists MK-7300.2016.2. We are indebted to Vladimir Dmitriev, Herman Emerich, Wouter van Beek, and Michela Brunelli for the friendly and competent support during the experiment performed at the BM01B (now BM31) beamline of the ESRF. We also thank Michele Carosso for the help in volumetric measurements. We acknowledge the stimulating and constructive comments of the referees who suggested us to extend the EXAFS analysis up to the third coordination shell (Section 4.3).

Author information

The authors declare no competing financial interests. Correspondence and requests for materials should be addressed to ALB (abugaev@sfedu.ru) or CL (carlo.lamberti@unito.it)

Supporting information

The Supporting Information is available free of charge via the Internet at <http://pubs.acs.org>. TEM details, EXAFS analysis, XRPD data, Rietveld refinement details, Williamson-Hall analysis, Volumetric measurements details.

References

- (1) Beletskaya, I. P.; Cheprakov, A. V. The Heck Reaction as a Sharpening Stone of Palladium Catalysis. *Chem. Rev.* **2000**, *100*, 3009-3066.
- (2) Lu, Z. H.; Liu, G. J.; Phillips, H.; Hill, J. M.; Chang, J.; Kydd, R. A. Palladium Nanoparticle Catalyst Prepared in Poly(Acrylic Acid)-Lined Channels of Diblock Copolymer Microspheres. *Nano Lett.* **2001**, *1*, 683-687.
- (3) Gopidas, K. R.; Whitesell, J. K.; Fox, M. A. Synthesis, Characterization, and Catalytic Applications of a Palladium-Nanoparticle-Cored Dendrimer. *Nano Lett.* **2003**, *3*, 1757-1760.
- (4) Barbaro, P.; Bianchini, C.; Dal Santo, V.; Meli, A.; Moneti, S.; Psaro, R.; Scaffidi, A.; Sordelli, L.; Vizza, F. Hydrogenation of Arenes Over Silica-Supported Catalysts that Combine a Grafted Rhodium Complex and Palladium Nanoparticles: Evidence for Substrate Activation on Rh Single-Site-Pd-Metal Moieties. *J. Am. Chem. Soc.* **2006**, *128*, 7065-7076.
- (5) Phan, N. T. S.; Van Der Sluys, M.; Jones, C. W. on The Nature of The Active Species in Palladium Catalyzed Mizoroki-Heck and Suzuki-Miyaura Couplings - Homogeneous or Heterogeneous Catalysis, a Critical Review. *Adv. Synth. Catal.* **2006**, *348*, 609-679.
- (6) Kantchev, E. A. B.; O'Brien, C. J.; Organ, M. G. Palladium Complexes of N-Heterocyclic Carbenes as Catalysts for Cross-Coupling Reactions - a Synthetic Chemist's Perspective. *Angew. Chem.-Int. Edit.* **2007**, *46*, 2768-2813.
- (7) Yin, L. X.; Liebscher, J. Carbon-Carbon Coupling Reactions Catalyzed by Heterogeneous Palladium Catalysts. *Chem. Rev.* **2007**, *107*, 133-173.
- (8) Park, J. N.; forman, A. J.; Tang, W.; Cheng, J. H.; Hu, Y. S.; Lin, H. F.; Mcfarland, E. W. Highly Active and Sinter-Resistant Pd-Nanoparticle Catalysts Encapsulated in Silica. *Small* **2008**, *4*, 1694-1697.
- (9) Li, Y.; Fan, X. B.; Qi, J. J.; Ji, J. Y.; Wang, S. L.; Zhang, G. L.; Zhang, F. B. Palladium Nanoparticle-Graphene Hybrids as Active Catalysts for the Suzuki Reaction. *Nano Res.* **2010**, *3*, 429-437.
- (10) Xu, X.; Li, Y.; Gong, Y. T.; Zhang, P. F.; Li, H. R.; Wang, Y. Synthesis of Palladium Nanoparticles Supported on Mesoporous N-Doped Carbon and their Catalytic Ability for Biofuel Upgrade. *J. Am. Chem. Soc.* **2012**, *134*, 16987-16990.
- (11) Pun, D.; Diao, T. N.; Stahl, S. S. Aerobic Dehydrogenation of Cyclohexanone to Phenol Catalyzed by Pd(TFA)₂/2-Dimethylaminopyridine: Evidence for the Role of Pd Nanoparticles. *J. Am. Chem. Soc.* **2013**, *135*, 8213-8221.
- (12) Lei, Y.; Lu, J.; Luo, X. Y.; Wu, T. P.; Du, P.; Zhang, X. Y.; Ren, Y.; Wen, J. G.; Miller, D. J., *et al.* Synthesis of Porous Carbon Supported Palladium Nanoparticle Catalysts by Atomic Layer Deposition: Application for Rechargeable Lithium-O₂ Battery. *Nano Lett.* **2013**, *13*, 4182-4189.

- (13) Jie, X. M.; Shang, Y. P.; Hu, P.; Su, W. P. Palladium-Catalyzed Oxidative Cross-Coupling between Heterocycles and Terminal Alkynes with low Catalyst Loading. *Angew. Chem.-Int. Edit.* **2013**, *52*, 3630-3633.
- (14) Chinchilla, R.; Najera, C. Chemicals from Alkynes with Palladium Catalysts. *Chem. Rev.* **2014**, *114*, 1783-1826.
- (15) Deraedt, C.; Astruc, D. "Homeopathic" Palladium Nanoparticle Catalysis of Cross Carbon-Carbon Coupling Reactions. *Accounts Chem. Res.* **2014**, *47*, 494-503.
- (16) Zhu, Q. L.; Tsumori, N.; Xu, Q. Immobilizing Extremely Catalytically Active Palladium Nanoparticles to Carbon Nanospheres: a Weakly-Capping Growth Approach. *J. Am. Chem. Soc.* **2015**, *137*, 11743-11748.
- (17) Mondal, B.; Acharyya, K.; Howlader, P.; Mukherjee, P. S. Molecular Cage Impregnated Palladium Nanoparticles: Efficient, Additive-Free Heterogeneous Catalysts for Cyanation of Aryl Halides. *J. Am. Chem. Soc.* **2016**, *138*, 1709-1716.
- (18) Rahimi, F.; Zad, A. I. Characterization of Pd Nanoparticle Dispersed over Porous Silicon as a Hydrogen Sensor. *J. Phys. D-Appl. Phys.* **2007**, *40*, 7201-7209.
- (19) Sugawa, K.; Tahara, H.; Yamashita, A.; Otsuki, J.; Sagara, T.; Harumoto, T.; Yanagida, S. Refractive Index Susceptibility of the Plasmonic Palladium Nanoparticle: Potential as the third Plasmonic Sensing Material. *ACS Nano* **2015**, *9*, 1895-1904.
- (20) Huang, J. S.; Liu, Y.; Hou, H. Q.; You, T. Y. Simultaneous Electrochemical Determination of Dopamine, Uric Acid and Ascorbic Acid Using Palladium Nanoparticle-Loaded Carbon Nanofibers Modified Electrode. *Biosens. Bioelectron.* **2008**, *24*, 632-637.
- (21) Huang, J. S.; Wang, D. W.; Hou, H. Q.; You, T. Y. Electrospun Palladium Nanoparticle-Loaded Carbon Nanofibers and their Electrocatalytic Activities towards Hydrogen Peroxide and NADH. *Adv. Funct. Mater.* **2008**, *18*, 441-448.
- (22) Lu, L. M.; Li, H. B.; Qu, F. L.; Zhang, X. B.; Shen, G. L.; Yu, R. Q. in Situ Synthesis of Palladium Nanoparticle-Graphene Nanohybrids and their Application in Nonenzymatic Glucose Biosensors. *Biosens. Bioelectron.* **2011**, *26*, 3500-3504.
- (23) Zeng, Q.; Cheng, J. S.; Liu, X. F.; Bai, H. T.; Jiang, J. H. Palladium Nanoparticle/Chitosan-Grafted Graphene Nanocomposites for Construction of a Glucose Biosensor. *Biosens. Bioelectron.* **2011**, *26*, 3456-3463.
- (24) Wang, H.; Zhang, Y.; Li, H.; Du, B.; Ma, H. M.; Wu, D.; Wei, Q. A Silver-Palladium Alloy Nanoparticle-Based Electrochemical Biosensor for Simultaneous Detection of Ractopamine, Clenbuterol and Salbutamol. *Biosens. Bioelectron.* **2013**, *49*, 14-19.
- (25) Gao, D. F.; Zhou, H.; Wang, J.; Miao, S.; Yang, F.; Wang, G. X.; Wang, J. G.; Bao, X. H. Size-Dependent Electrocatalytic Reduction of CO₂ over Pd Nanoparticles. *J. Am. Chem. Soc.* **2015**, *137*, 4288-4291.
- (26) Armbrüster, M.; Behrens, M.; Cinquini, F.; Föttinger, K.; Grin, Y.; Haghofer, A.; Klötzer, B.; Knop-Gericke, A.; Lorenz, H., *et al.* How to Control the Selectivity of Palladium-Based Catalysts in Hydrogenation Reactions: the Role of Subsurface Chemistry. *Chemcatchem* **2012**, *4*, 1048-1063.
- (27) Borodziński, A.; Bond, G. C. Selective Hydrogenation of Ethyne in Ethene-Rich Streams on Palladium Catalysts, Part 2: Steady-State Kinetics and Effects of Palladium Particle Size, Carbon Monoxide, and Promoters. *Cat. Rev. - Sci. Eng.* **2008**, *50*, 379-469.
- (28) Borodziński, A.; Bond, G. C. Selective Hydrogenation of Ethyne in Ethene-Rich Streams on Palladium Catalysts. Part 1. Effect of Changes to the Catalyst During Reaction. *Cat. Rev. - Sci. Eng.* **2006**, *48*, 91-144.
- (29) Borodziński, A. The Effect of Palladium Particle Size on the Kinetics of Hydrogenation of Acetylene-Ethylene Mixtures Over Pd/SiO₂ Catalysts. *Catal. Lett.* **2001**, *71*, 169-175.
- (30) Molnar, A.; Sarkany, A.; Varga, M. Hydrogenation of Carbon-Carbon Multiple Bonds: Chemo-, Regio- and Stereo-Selectivity. *J. Mol. Catal. A-Chem.* **2001**, *173*, 185-221.
- (31) Tew, M. W.; Nachtegaal, M.; Janousch, M.; Huthwelker, T.; Van Bokhoven, J. A. The Irreversible formation of Palladium Carbide During Hydrogenation of 1-Pentyne Over Silica-Supported Palladium Nanoparticles: in Situ Pd K and L₃ Edge XAS. *Phys. Chem. Chem. Phys.* **2012**, *14*, 5761-5768.
- (32) Tew, M. W.; Janousch, M.; Huthwelker, T.; Van Bokhoven, J. A. The Roles of Carbide and Hydride in Oxide-Supported Palladium Nanoparticles for Alkyne Hydrogenation. *J. Catal.* **2011**, *283*, 45-54.
- (33) Moreno-Manas, M.; Pleixats, R. formation of Carbon-Carbon Bonds Under Catalysis by Transition-Metal Nanoparticles. *Accounts Chem. Res.* **2003**, *36*, 638-643.
- (34) Pellegrini, R.; Agostini, G.; Groppo, E.; Piovano, A.; Leofanti, G.; Lamberti, C. 0.5 Wt.% Pd/C Catalyst for Purification of Terephthalic Acid: Irreversible Deactivation in Industrial Plants. *J. Catal.* **2011**, *280*, 150-160.
- (35) Berube, V.; Radtke, G.; Dresselhaus, M.; Chen, G. Size Effects on the Hydrogen Storage Properties of Nanostructured Metal Hydrides: a Review. *Int. J. Energy Res.* **2007**, *31*, 637-663.
- (36) Griessen, R.; Strohfeltdt, N.; Giessen, H. thermodynamics of the Hybrid Interaction of Hydrogen with Palladium Nanoparticles. *Nat. Mater.* **2016**, *15*, 311-317.
- (37) Jovic, H.; Renouprez, A. formation of Hydrides in Small Particles of Palladium Supported in Y-Zeolite. *J. Less-Common Met.* **1987**, *129*, 311-316.

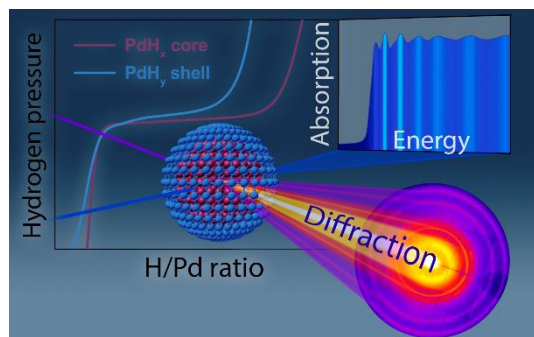
- (38) Johansson, M.; Skulason, E.; Nielsen, G.; Murphy, S.; Nielsen, R. M.; Chorkendorff, I. Hydrogen Adsorption on Palladium and Palladium Hydride at 1 Bar. *Surf. Sci.* **2010**, *604*, 718-729.
- (39) Kishore, S.; Nelson, J. A.; Adair, J. H.; Eklund, P. C. Hydrogen Storage in Spherical and Platelet Palladium Nanoparticles. *J. Alloy. Compd.* **2005**, *389*, 234-242.
- (40) Langhammer, C.; Zhdanov, V. P.; Zoric, I.; Kasemo, B. Size-Dependent Hysteresis in the formation and Decomposition of Hydride in Metal Nanoparticles. *Chem. Phys. Lett.* **2010**, *488*, 62-66.
- (41) Mccaulley, J. A. in-Situ X-Ray Absorption Spectroscopy Studies of Hydride and Carbide formation in Supported Palladium Catalysts. *J. Phys. Chem.* **1993**, *97*, 10372-10379.
- (42) Nag, N. K. a Study on the formation of Palladium Hydride in a Carbon-Supported Palladium Catalyst. *J. Phys. Chem. B* **2001**, *105*, 5945-5949.
- (43) Shegai, T.; Langhammer, C. Hydride formation in Single Palladium and Magnesium Nanoparticles Studied by Nanoplasmonic Dark-Field Scattering Spectroscopy. *Adv. Mater.* **2011**, *23*, 4409-4414.
- (44) Soldatov, A.; Della Longa, S.; Bianconi, A. Relevant Role of Hydrogen atoms in the XANES of Pd Hydride: Evidence of Hydrogen Induced Unoccupied States. *Solid State Commun.* **1993**, *85*, 863-868.
- (45) Syrenova, S.; Wadell, C.; Nugroho, F. A. A.; Gschneidner, T. A.; Fernandez, Y. A. D.; Nalin, G.; Switlik, D.; Westerlund, F.; Antosiewicz, T. J., *et al.* Hydride formation thermodynamics and Hysteresis in Individual Pd Nanocrystals with Different Size and Shape. *Nat. Mater.* **2015**, *14*, 1236-1244.
- (46) Wadell, C.; Pingel, T.; Olsson, E.; Zoric, I.; Zhdanov, V. P.; Langhammer, C. thermodynamics of Hydride formation and Decomposition in Supported sub-10 nm Pd Nanoparticles of Different Sizes. *Chem. Phys. Lett.* **2014**, *603*, 75-81.
- (47) Bauer, M.; Schoch, R.; Shao, L.; Zhang, B.; Knop-Gericke, A.; Willinger, M.; Schlögl, R.; Teschner, D. Structure-Activity Studies on Highly Active Palladium Hydrogenation Catalysts by X-Ray Absorption Spectroscopy. *J. Phys. Chem. C* **2012**, *116*, 22375-22385.
- (48) Bugaev, A. L.; Guda, A. A.; Lazzarini, A.; Lomachenko, K. A.; Groppo, E.; Pellegrini, R.; Piovano, A.; Emerich, H.; Soldatov, A. V., *et al.* In Situ formation of Hydrides and Carbides in Palladium Catalyst: When XANES is Better than EXAFS and XRD. *Catal. today* **2017**, *283*, 119-126.
- (49) Teschner, D.; Borsodi, J.; Wootsch, A.; Revay, Z.; Havecker, M.; Knop-Gericke, A.; Jackson, S. D.; Schlögl, R. The Roles of Subsurface Carbon and Hydrogen in Palladium-Catalyzed Alkyne Hydrogenation. *Science* **2008**, *320*, 86-89.
- (50) Teschner, D.; Borsodi, J.; Kis, Z.; Szentmiklósi, L.; Révay, Z.; Knop-Gericke, A.; Schlögl, R.; Torres, D.; Sautet, P. Role of Hydrogen Species in Palladium-Catalyzed Alkyne Hydrogenation. *J. Phys. Chem. C* **2010**, *114*, 2293-2299.
- (51) Lewis, F. A. the Palladium-Hydrogen System. *Platin. Met. Rev.* **1982**, *26*, 70-78.
- (52) Langhammer, C.; Larsson, E. M.; Kasemo, B.; Zoric, I. Indirect Nanoplasmonic Sensing: Ultrasensitive Experimental Platform for Nanomaterials Science and Optical Nanocalorimetry. *Nano Lett.* **2010**, *10*, 3529-3538.
- (53) Ingham, B.; toney, M. F.; Hendy, S. C.; Cox, T.; Fong, D. D.; Eastman, J. A.; Fuoss, P. H.; Stevens, K. J.; Lassesson, A., *et al.* Particle Size Effect of Hydrogen-Induced Lattice Expansion of Palladium Nanoclusters. *Phys. Rev. B* **2008**, *78*, Art. N. 245408.
- (54) Narehood, D.; Kishore, S.; Goto, H.; Adair, J.; Nelson, J.; Gutierrez, H.; Eklund, P. X-Ray Diffraction and H-Storage in Ultra-Small Palladium Particles. *Int. J. Hydrogen Energ.* **2009**, *34*, 952-960.
- (55) Rehr, J. J.; Albers, R. C. Theoretical Approaches to X-Ray Absorption Fine Structure. *Rev. Mod. Phys.* **2000**, *72*, 621-654.
- (56) Chiarello, G. L.; Ferri, D. Modulated Excitation Extended X-Ray Absorption Fine Structure Spectroscopy. *Phys. Chem. Chem. Phys.* **2015**, *17*, 10579-10591.
- (57) Ferri, D.; Kumar, M. S.; Wirz, R.; Eyssler, A.; Korsak, O.; Hug, P.; Weidenkaff, A.; Newton, M. A. First Steps in Combining Modulation Excitation Spectroscopy with Synchronous Dispersive EXAFS/DRIFTS/Mass Spectrometry for in Situ Time Resolved Study of Heterogeneous Catalysts. *Phys. Chem. Chem. Phys.* **2010**, *12*, 5634-5646.
- (58) Ferri, D.; Newton, M. A.; Di Michiel, M.; Chiarello, G. L.; Yoon, S.; Lu, Y.; Andrieux, J. Revealing the Dynamic Structure of Complex Solid Catalysts Using Modulated Excitation X-Ray Diffraction. *Angew. Chem.-Int. Ed.* **2014**, *53*, 8890-8894.
- (59) Frenkel, A. I.; Hills, C. W.; Nuzzo, R. G. a View From the Inside: Complexity in the atomic Scale Ordering of Supported Metal Nanoparticles. *J. Phys. Chem. B* **2001**, *105*, 12689-12703.
- (60) Frenkel, A. I.; Yevick, A.; Cooper, C.; Vasic, R. Modeling the Structure and Composition of Nanoparticles by Extended X-Ray Absorption Fine-Structure Spectroscopy. *Ann. Rev. Anal. Chem.* **2011**, *4*, 23-39.
- (61) Frenkel, A. I. Applications of Extended X-Ray Absorption Fine-Structure Spectroscopy to Studies of Bimetallic Nanoparticle Catalysts. *Chem. Soc. Rev.* **2012**, *41*, 8163-8178.
- (62) Agostini, G.; Pellegrini, R.; Leofanti, G.; Bertinetti, L.; Bertarione, S.; Groppo, E.; Zecchina, A.; Lamberti, C. Determination of the Particle Size, Available Surface Area, and Nature of Exposed Sites for Silica-Alumina-Supported Pd Nanoparticles: a Multitechnical Approach. *J. Phys. Chem. C* **2009**, *113*, 10485-10492.

- (63) Agostini, G.; Piovano, A.; Bertinetti, L.; Pellegrini, R.; Leofanti, G.; Groppo, E.; Lamberti, C. Effect of Different Face Centered Cubic Nanoparticle Distributions on Particle Size and Surface Area Determination: a Theoretical Study. *J. Phys. Chem. C* **2014**, *118*, 4085-4094.
- (64) Van Bokhoven, J. A.; Lamberti, C., *X-Ray Absorption and X-Ray Emission Spectroscopy: Theory and Applications*. Wiley & Sons: Chichester, 2016.
- (65) Mino, L.; Agostini, G.; Borfecchia, E.; Gianolio, D.; Piovano, A.; Gallo, E.; Lamberti, C. Low-Dimensional Systems Investigated by X-Ray Absorption Spectroscopy: a Selection of 2D, 1D and 0D Cases. *J. Phys. D: Appl. Phys.* **2013**, *46*, Art. N. 423001.
- (66) Bordiga, S.; Groppo, E.; Agostini, G.; Van Bokhoven, J. A.; Lamberti, C. Reactivity of Surface Species in Heterogeneous Catalysts Probed by in Situ X-Ray Absorption Techniques. *Chem. Rev.* **2013**, *113*, 1736-1850.
- (67) Manzoli, M.; Vindigni, F.; Tabakova, T.; Lamberti, C.; Dimitrov, D.; Ivanov, K.; Agostini, G. Structure-Reactivity Relationship in Co_3O_4 Promoted Au/ CeO_2 Catalysts for the CH_3OH Oxidation Reaction Revealed by in Situ FTIR and Operando EXAFS Studies. *J. Mater. Chem. A* **2017**, *5*, 2083-2094.
- (68) Bugaev, A. L.; Guda, A. A.; Lomachenko, K. A.; Lazzarini, A.; Srabionyan, V. V.; Vitillo, J. G.; Piovano, A.; Groppo, E.; Bugaev, L. A., *et al.* Hydride Phase formation in Carbon Supported Palladium Hydride Nanoparticles by in Situ EXAFS and XRD. *J. Phys. Conf. Ser.* **2016**, *712*, Art. N. 012032.
- (69) Campesi, R.; Cuevas, F.; Gadiou, R.; Leroy, E.; Hirscher, M.; Vix-Guterl, C.; Latroche, M. Hydrogen Storage Properties of Pd Nanoparticle/Carbon Template Composites. *Carbon* **2008**, *46*, 206-214.
- (70) Srabionyan, V. V.; Bugaev, A. L.; Pryadchenko, V. V.; Avakyan, L. A.; Van Bokhoven, J. A.; Bugaev, L. A. EXAFS Study of Size Dependence of atomic Structure in Palladium Nanoparticles. *J. Phys. Chem. Solids* **2014**, *75*, 470-476.
- (71) Zlotea, C.; Cuevas, F.; Paul-Boncour, V.; Leroy, E.; Dibandjo, P.; Gadiou, R.; Vix-Guterl, C.; Latroche, M. Size-Dependent Hydrogen Sorption in Ultrasmall Pd Clusters Embedded in a Mesoporous Carbon Template. *J. Am. Chem. Soc.* **2010**, *132*, 7720-7729.
- (72) Poncelet, G.; Jacobs, P.; Grange, P., *Preparation of Catalysts III*. Elsevier: 1983; Vol. 16.
- (73) Piovano, A.; Lazzarini, A.; Pellegrini, R.; Leofanti, G.; Agostini, G.; Rudić, S.; Bugaev, A. L.; Lamberti, C.; Groppo, E. Progress in the Characterization of the Surface Species in Activated Carbons by Means of INS Spectroscopy Coupled with Detailed DFT Calculations. *Adv. Cond. Matter Phys.* **2015**, *2015*, 1-8.
- (74) Agostini, G.; Lamberti, C.; Pellegrini, R.; Leofanti, G.; Giannici, F.; Longo, A.; Groppo, E. Effect of Pre-Reduction on the Properties and the Catalytic Activity of Pd/Carbon Catalysts: a Comparison with Pd/ Al_2O_3 . *ACS Catal.* **2014**, *4*, 187-194.
- (75) Van Beek, W.; Safonova, O. V.; Wiker, G.; Emerich, H. SNBL, a Dedicated Beamline for Combined in Situ X-Ray Diffraction, X-Ray Absorption and Raman Scattering Experiments. *Phase Transit.* **2011**, *84*, 726-732.
- (76) Abdala, P. M.; Safonova, O. V.; Wiker, G.; Van Beek, W.; Emerich, H.; Van Bokhoven, J. A.; Sa, J.; Szlachetko, J.; Nachtegaal, M. Scientific Opportunities for Heterogeneous Catalysis Research at the Superxas and SNBL Beam Lines. *Chimia* **2012**, *66*, 699-705.
- (77) Groppo, E.; Agostini, G.; Piovano, A.; Muddada, N. B.; Leofanti, G.; Pellegrini, R.; Portale, G.; Longo, A.; Lamberti, C. Effect of Reduction in Liquid Phase on the Properties and the Catalytic Activity of Pd/ Al_2O_3 Catalysts. *J. Catal.* **2012**, *287*, 44-54.
- (78) Ravel, B.; Newville, M. ATHENA, ARTEMIS, HEPHAESTUS: Data Analysis for X-Ray Absorption Spectroscopy Using IFEFFIT. *J. Synchrotron Radiat.* **2005**, *12*, 537-541.
- (79) Calvin, S.; Miller, M. M.; Goswami, R.; Cheng, S. F.; Mulvaney, S. P.; Whitman, L. J.; Harris, V. G. Determination of Crystallite Size in a Magnetic Nanocomposite Using Extended X-Ray Absorption Fine Structure. *J Appl Phys* **2003**, *94*, 778-783.
- (80) Groppo, E.; Prestipino, C.; Lamberti, C.; Luches, P.; Giovanardi, C.; Boscherini, F. Growth of NiO on Ag(001): atomic Environment, Strain, and Interface Relaxations Studied by Polarization Dependent Extended X-Ray Absorption Fine Structure. *J. Phys. Chem. B* **2003**, *107*, 4597-4606.
- (81) Borfecchia, E.; Maurelli, S.; Gianolio, D.; Groppo, E.; Chiesa, M.; Bonino, F.; Lamberti, C. Insights into Adsorption of NH_3 on HKUST-1 Metal-Organic Framework: a Multitechnique Approach. *J. Phys. Chem. C* **2012**, *116*, 19839-19850.
- (82) Borfecchia, E.; Lomachenko, K. A.; Giordanino, F.; Falsig, H.; Beato, P.; Soldatov, A. V.; Bordiga, S.; Lamberti, C. Revisiting the Nature of Cu Sites in the Activated Cu-SSZ-13 Catalyst for SCR Reaction. *Chem. Sci.* **2015**, *6*, 548-563.
- (83) Zabinsky, S. I.; Rehr, J. J.; Ankudinov, A.; Albers, R. C.; Eller, M. J. Multiple-Scattering Calculations of X-Ray-Absorption Spectra. *Phys. Rev. B* **1995**, *52*, 2995-3009.
- (84) Kieffer, J.; Wright, J. P. Pyfai: a Python Library for High Performance Azimuthal Integration on GPU. *Powder Diffract.* **2013**, *28*, S339-S350.
- (85) Petříček, V.; Dušek, M.; Palatinus, L. Crystallographic Computing System JANA2006: General Features. *Z. Kristallog.* **2014**, *229*, 345-352.

- (86) Zuttel, A.; Nutzenadel, C.; Schmid, G.; Emmenegger, C.; Sudan, P.; Schlapbach, L. thermodynamic Aspects of the Interaction of Hydrogen with Pd Clusters. *Appl. Surf. Sci.* **2000**, *162*, 571-575.
- (87) Eastman, J. A.; Thompson, L. J.; Kestel, B. J. Narrowing of the Palladium-Hydrogen Miscibility Gap in Nanocrystalline Palladium. *Phys. Rev. B* **1993**, *48*, 84-92.
- (88) Langhammer, C.; Zhdanov, V. P.; Zorić, I.; Kasemo, B. Size-Dependent Kinetics of Hydriding and Dehydriding of Pd Nanoparticles. *Phys. Rev. Lett.* **2010**, *104*, Art. N. 135502.
- (89) Pundt, A.; Suleiman, M.; Bahtz, C.; Reetz, M. T.; Kirchheim, R.; Jisrawi, N. M. Hydrogen and Pd-Clusters. *Mater. Sci. Eng. B-Solid State Mater. Adv. Technol.* **2004**, *108*, 19-23.
- (90) Sachs, C.; Pundt, A.; Kirchheim, R.; Winter, M.; Reetz, M. T.; Fritsch, D. Solubility of Hydrogen in Single-Sized Palladium Clusters. *Phys. Rev. B* **2001**, *64*, Art. N. 075408.
- (91) Suleiman, M.; Faupel, J.; Borchers, C.; Krebs, H. U.; Kirchheim, R.; Pundt, A. Hydrogen Absorption Behaviour in Nanometer Sized Palladium Samples Stabilised in Soft and Hard Matrix. *J. Alloy. Compd.* **2005**, *404*, 523-528.
- (92) Suleiman, M.; Jisrawi, N. M.; Dankert, O.; Reetz, M. T.; Bahtz, C.; Kirchheim, R.; Pundt, A. Phase Transition and Lattice Expansion During Hydrogen Loading of Nanometer Sized Palladium Clusters. *J. Alloy. Compd.* **2003**, *356*, 644-648.
- (93) Yamauchi, M.; Ikeda, R.; Kitagawa, H.; Takata, M. Nanosize Effects on Hydrogen Storage in Palladium. *J. Phys. Chem. C* **2008**, *112*, 3294-3299.
- (94) Yamauchi, M.; Kitagawa, H. Hydrogen Absorption of the Polymer-Coated Pd Nanoparticle. *Synth. Met.* **2005**, *153*, 353-356.
- (95) Flanagan, T. B.; Oates, W. A. the Palladium-Hydrogen System. *Annu. Rev. Mater. Sci.* **1991**, *21*, 269-304.
- (96) Baldi, A.; Narayan, T. C.; Koh, A. L.; Dionne, J. A. In Situ Detection of Hydrogen-Induced Phase Transitions in Individual Palladium Nanocrystals. *Nat. Mater.* **2014**, *13*, 1143-1148.
- (97) Bardhan, R.; Hedges, L. O.; Pint, C. L.; Javey, A.; Whitlam, S.; Urban, J. J. Uncovering the Intrinsic Size Dependence of Hydriding Phase Transformations in Nanocrystals. *Nat. Mater.* **2013**, *12*, 905-912.
- (98) Fischer, F. D.; Waitz, T.; Vollath, D.; Simha, N. K. On the Role of Surface Energy and Surface Stress in Phase-Transforming Nanoparticles. *Prog. Mater. Sci.* **2008**, *53*, 481-527.
- (99) Ren, H.; Zhang, T.-Y. H Concentrations and Stresses in Pd Nanoparticles. *Matter. Lett.* **2014**, *130*, 176-179.
- (100) Zhdanov, V. P.; Kasemo, B. Kinetics of the formation of a New Phase in Nanoparticles. *Chem. Phys. Lett.* **2008**, *460*, 158-161.
- (101) Braglia, L.; Borfecchia, E.; Lomachenko, K. A.; Bugaev, A. L.; Guda, A. A.; Soldatov, A. V.; Bleken, B. T. L.; Oien, S.; Olsbye, U., *et al.* Tuning Pt and Cu Sites Population Inside Functionalized UiO-67 MOF by Controlling Activation Conditions. *Faraday Discuss.* **2017**, DOI: 10.1039/C1037FD00024C.
- (102) Borfecchia, E.; Gianolio, D.; Agostini, G.; Bordiga, S.; Lamberti, C., Characterization of MOFs. 2. Long and Local Range Order Structural Determination of MOFs by Combining EXAFS and Diffraction Techniques. in *Metal Organic Frameworks as Heterogeneous Catalysts*, Llabrés I Xamena, F.; Gascón, J., Eds. the Royal Society of Chemistry: Cambridge: Cambridge, 2013; Pp 143-208.
- (103) Fornasini, P.; Grisenti, R. on EXAFS Debye-Waller Factor and Recent Advances. *J. Synchrotron Radiat.* **2015**, *22*, 1242-1257.
- (104) Lebedev, A. I.; Sluchinskaya, I. A.; Demin, V. N.; Munro, I. EXAFS Studies of the Local Environment of Lead and Selenium atoms in $\text{PbTe}_{1-x}\text{Se}_x$ Solid Solutions. *Phys. Sol. State* **1999**, *41*, 1275-1282.
- (105) Razmara, M. F.; Henderson, C. M. B.; Patrick, R. A. D.; Bell, A. M. T.; Charnock, J. M. the Crystal Chemistry of the Solid Solution Series Between Chalcostibite (CuSbS_2) and Emplectite (CuBiS_2). *Mineral. Mag.* **1997**, *61*, 79-88.
- (106) Kuzmin, A.; Mironova, N.; Purans, J.; Sazonov, A. EXAFS and XANES Studies of $\text{Co}_x\text{Mg}_{1-x}\text{O}$ Solid Solutions Using a Laboratory EXAFS Spectrometer. *Phys. Status Solidi a* **1993**, *135*, 133-141.
- (107) Romanato, F.; De Salvador, D.; Berti, M.; Drigo, A.; Natali, M.; tormen, M.; Rossetto, G.; Pascarelli, S.; Boscherini, F., *et al.* Bond-Length Variation in $\text{In}_x\text{Ga}_{1-x}\text{As}/\text{InP}$ Strained Epitaxial Layers. *Phys. Rev. B* **1998**, *57*, 14619-14622.
- (108) Bugaev, L. A.; Avakyan, L. A.; Srabionyan, V. V.; Bugaev, A. L. Resolution of Interatomic Distances in the Study of Local atomic Structure Distortions by Energy-Restricted X-Ray Absorption Spectra. *Phys. Rev. B* **2010**, *82*, Art. N. 064204.
- (109) Lv, C. Q.; Ling, K. C.; Wang, G. C. Methane Combustion on Pd-Based Model Catalysts: Structure Sensitive or Insensitive? *J. Chem. Phys.* **2009**, *131*, Art. N. 144704.
- (110) Van Santen, R. A. Complementary Structure Sensitive and Insensitive Catalytic Relationships. *Accounts Chem. Res.* **2009**, *42*, 57-66.
- (111) Sanchez-Sanchez, C. M.; Solla-Gullon, J.; Vidal-Iglesias, F. J.; Aldaz, A.; Montiel, V.; Herrero, E. Imaging Structure Sensitive Catalysis on Different Shape-Controlled Platinum Nanoparticles. *J. Am. Chem. Soc.* **2010**, *132*, 5622-5624.
- (112) Childers, D. J.; Schweitzer, N. M.; Shahari, S. M. K.; Rioux, R. M.; Miller, J. T.; Meyer, R. J. Modifying Structure-Sensitive Reactions by Addition of Zn to Pd. *J. Catal.* **2014**, *318*, 75-84.

(113) Li, Y. F.; Cui, F.; Ross, M. B.; Kim, D.; Sun, Y.; Yang, P. D. Structure-Sensitive CO₂ Electroreduction to Hydrocarbons on Ultrathin 5-Fold Twinned Copper Nanowires. *Nano Lett.* **2017**, *17*, 1312-1317.

TOC Graphic



Supporting information

Core-Shell Structure of Palladium Hydride Nanoparticles Revealed by Combined X-ray Absorption Spectroscopy and X-ray Diffraction

Aram L. Bugaev^{,†,‡}, Alexander A. Guda[†], Kirill A. Lomachenko^{†,§}, Viktor V. Shapovalov[†], Andrea Lazzarini^{‡,||}, Jenny G. Vitillo[‡], Lusegen A. Bugaev[†], Elena Groppo[‡], Riccardo Pellegrini[⊥], Alexander V. Soldatov[†], Jeroen A. van Bokhoven[#], Carlo Lamberti^{†,‡}*

[†]Smart Materials International Research Center, Southern Federal University, Sladkova 174/28, 344090 Rostov-on-Don, Russia

[‡]Department of Chemistry, University of Turin, Via P. Giuria 7, 10125 Turin, Italy

[§]European Synchrotron Radiation Facility, 71 avenue des Martyrs, 38043 Grenoble Cedex 9, France

^{||}inGAP Centre for Research Based Innovation, Department of Chemistry, University of Oslo, P.O. Box 1033, N-0315 Oslo, Norway

[⊥]Chimet SpA - Catalyst Division, Via di Pesciola 74, 52041 Vicinomaggo Arezzo, Italy

[#]Institute for Chemical and Bioengineering, ETH Zurich, Vladimir-Prelog-Weg 1, 8093 Zurich, Switzerland and Laboratory for Catalysis and Sustainable Chemistry, Paul Scherrer Institute, 5232 Villigen, Switzerland

e-mails: (abugaev@sfedu.ru ; carlo.lamberti@unito.it)

S1. TEM analysis.

TEM micrographs were taken by Jeol 3010-UHR microscope operated at 300 kV and equipped with a 2k × 2k pixels Gatan US1000 CCD camera. The particle size analysis was performed using ImageJ software by counting more than 500 particles. The representative TEM micrograph and obtained particle size distribution is shown in Figure S1, which duplicates the Figure 1 of the main text.

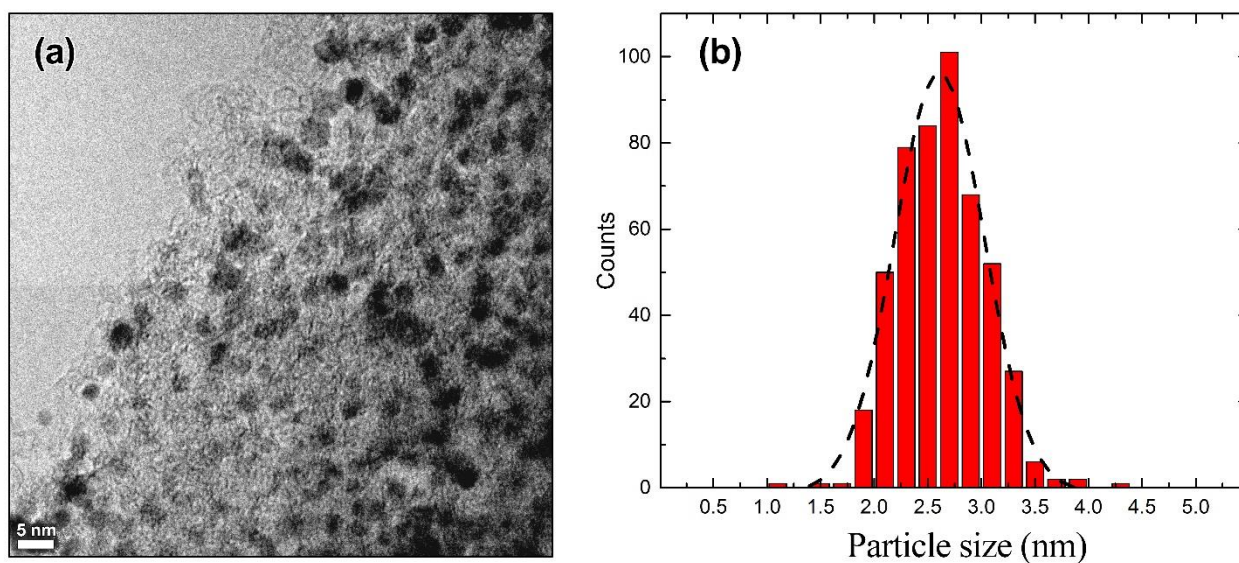


Figure S1. (a) TEM micrograph of 5%Pd/C sample. (b) Particle size distribution of palladium nanoparticles.

S2. EXAFS analysis

Formation of palladium hydride phase has two major effect on the X-ray absorption spectra. First, changes in the unoccupied electronic states of palladium induced by mixing with the unoccupied states of inserted hydrogen atoms¹⁻⁴ modifies the XANES part of the spectra (Figure S2a). Second, increase of the Pd-Pd interatomic distance results in the smaller period of EXAFS oscillations (Figure S2b). In the current work we focus on the Fourier-analysis of the EXAFS part. Single shell Fourier-analysis was performed using Demeter software.⁵ All spectra were aligned in energy according to the reference spectrum of palladium foil which was measured simultaneously at each step. Then, the E_0 energy was selected for each spectrum at the maximum of the first derivative. After background subtraction and normalization, the $\chi(R)$ functions were extracted for each spectrum (Figure S2b).

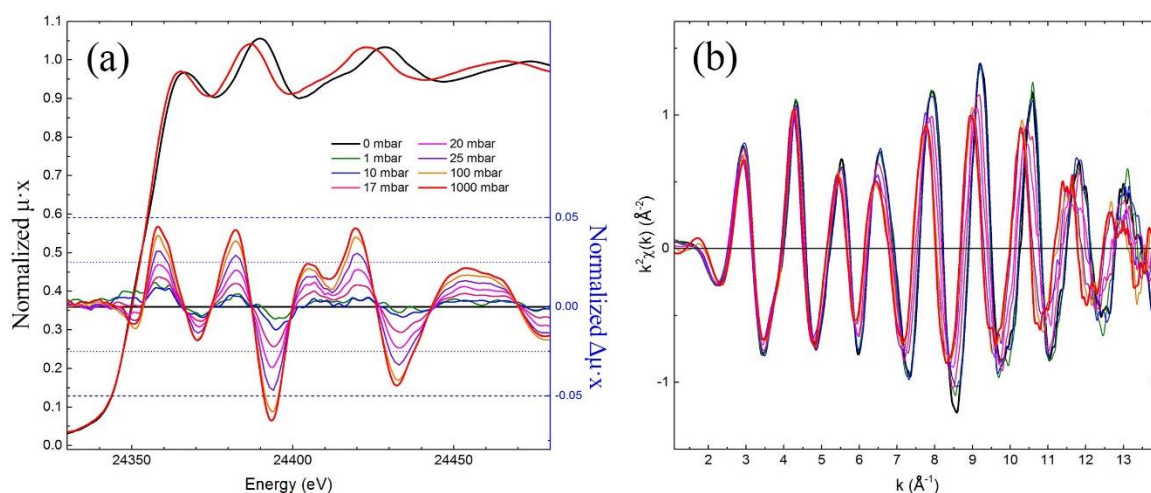


Figure S2. (a) Evolution of difference XANES spectra and (b) k^2 -weighted $\chi(k)$ oscillatory functions of EXAFS spectra taken during the hydride formation in palladium nanoparticles at 22 °C. For better visualization the spectra for only selected hydrogen pressure are shown.

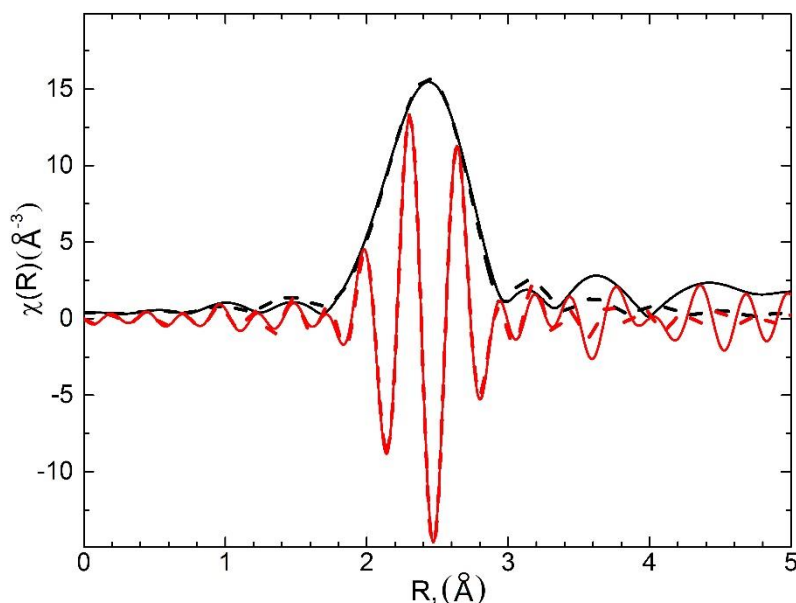


Figure S3. k^2 -weighted, phase uncorrected, Fourier-transform of EXAFS spectrum of bare palladium nanoparticles at 22 °C. Black and red solid lines correspond to the modulus and imaginary part of experimental $\chi(R)$ respectively, the first-shell best-fit data are shown by dashed lines.

The k -region for the analysis was taken from 5 to 12 \AA^{-1} . The region of $k < 5$ was excluded to reduce the possible contribution of the interaction of the palladium atoms with the support. To enhance the signal at large k , the data were weighted by k^2 . The Fourier-analysis of the spectrum of the palladium foil gave the value of the amplitude reduction factor $S_0^2 = 0.83 \pm 0.03$. This value was then fixed and used to determine the coordination number, N , for the spectra of the nanoparticles. At the first step, we checked that the coordination number does not change significantly in the whole range of the studied pressures and temperatures, and in the second step all spectra were analyzed simultaneously, and the value of coordination number was assumed to be the same for all spectra. This allowed us to decrease the number of variables and a correlation between coordination number N and Debye-Waller parameter, σ^2 . The obtained value of $N = 9.3 \pm 0.4$ is consistent with the average particle size.⁶ The two other fitting parameters were the zero energy shift, ΔE_0 , and the first shell Pd-Pd interatomic distance, $R_{\text{Pd-Pd}}$. The evolution of the $R_{\text{Pd-Pd}}$ was then used to plot pressure-distance isotherms shown in Figure 3a of the main text. The example of the fitted data in R space is shown in Figure S3.

The theoretical $\chi(k)$ functions of all scattering paths used for higher-shell EXAFS analysis are demonstrated in Figure S4. The corresponding $\chi(R)$ functions (here k -range from 3 to 14 \AA^{-1} was used) are shown in Figure S5.

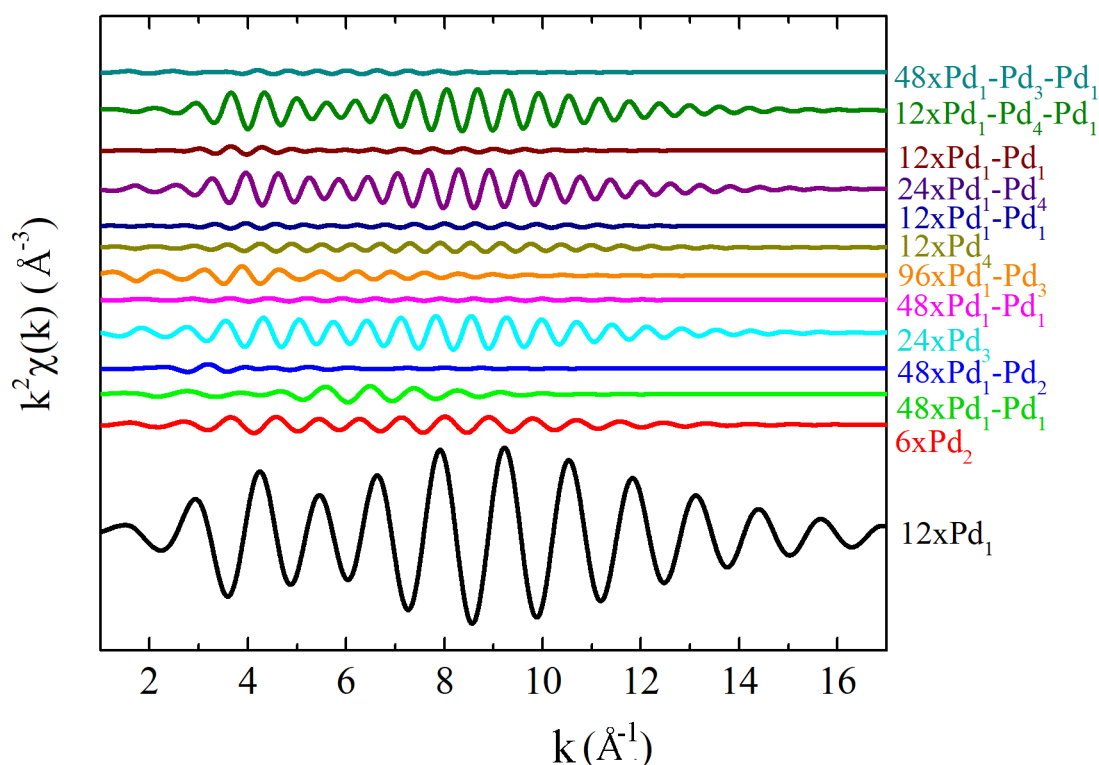


Figure S4. k^2 -weighted theoretical $\chi(k)$ functions for all scattering paths used in the higher-shell EXAFS fitting.

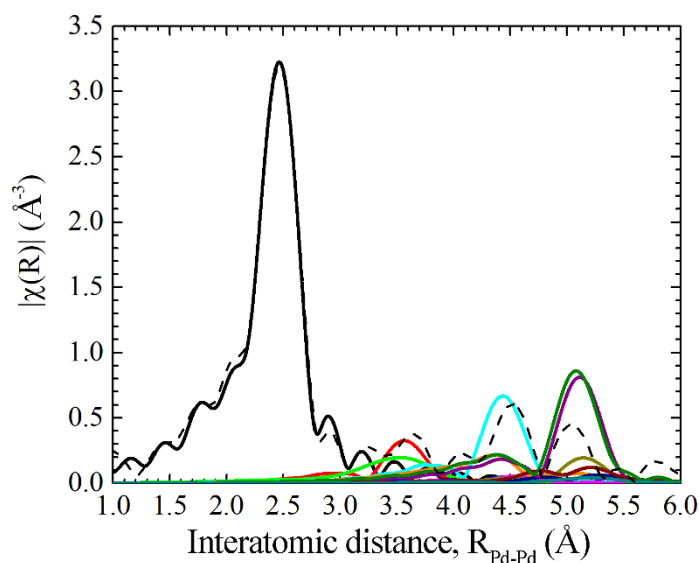


Figure S5. k^2 -weighted, phase uncorrected, Fourier-transform of each theoretical scattering path. The color-scheme is used the same as in Figure S4, dashed line corresponds to the experimental data for metallic palladium black.

S3. XRPD analysis

The quality of the experimental XRPD patterns can be appreciated in Figure S6, referred to the isotherm at 22 °C. XRPD patterns were analyzed using Jana2006 code.⁷ In order to reduce the number of variable parameters, at the first step we have performed Rietveld refinement for the initial and final points of each isotherm, which correspond to bare palladium (in vacuum) and β -hydride phase ($P_{H_2} = 1000$ mbar) respectively. The profile parameters obtained from these initial refinements were then fixed for the patterns corresponding to all intermediate steps, leaving only the following free

parameters: zero angle shift, cell parameters of α - and β - phases, and the relative concentration of α - and β - phases. At the final step the zero angle shift was fixed to the average value of the refined values obtained along the whole set of patterns, and the refinement procedure for all data was repeated. This procedure gives stability to the refined lattice parameters of the α - and β - phases (a_α and a_β , respectively). In order to allow, along the isotherms, a direct comparison between the average $R_{\text{Pd-Pd}}$ measured by EXAFS and the structural data obtained from Rietveld refinement (Figure 3 of the main text), the averaged cell parameter was calculated as a weighted sum: $a = (1 - n) \cdot a_\alpha + n \cdot a_\beta$, where n is a fraction of β -phase determined together with a_α and a_β by Rietveld refinement. Example of the refined XRPD pattern is illustrated in Fig.S5a.

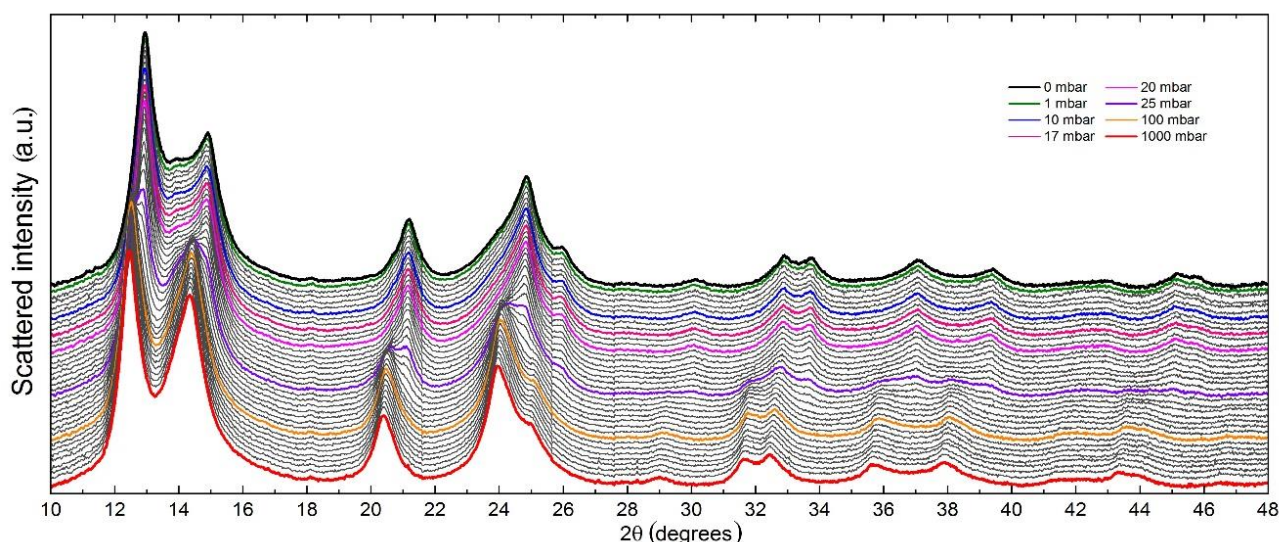


Figure S6. Evolution of XRPD patterns during hydride formation in the palladium nanoparticles at 22 °C. The patterns for the selected pressures are highlighted by colors as in the Figure S2.

Figure S7b shows how the cell parameters of the α - and β - phases, and the average cell parameter increase with increasing hydrogen pressure. Two phases were used in the refinement procedure even in the regions of hydrogen pressure below 1 mbar and above 100 mbar where only single phase is expected. As the result, the concentration of the β -phase in the low-pressure region of less than 5% was obtained which should be considered as a precision limit of the determination of phase concentration for this sample. Concentration of α -phase in the high pressure region was less than 2%. Due to high instability of a_α in the high pressure region its value was fixed for all patterns in the 30-1000 mbar range.

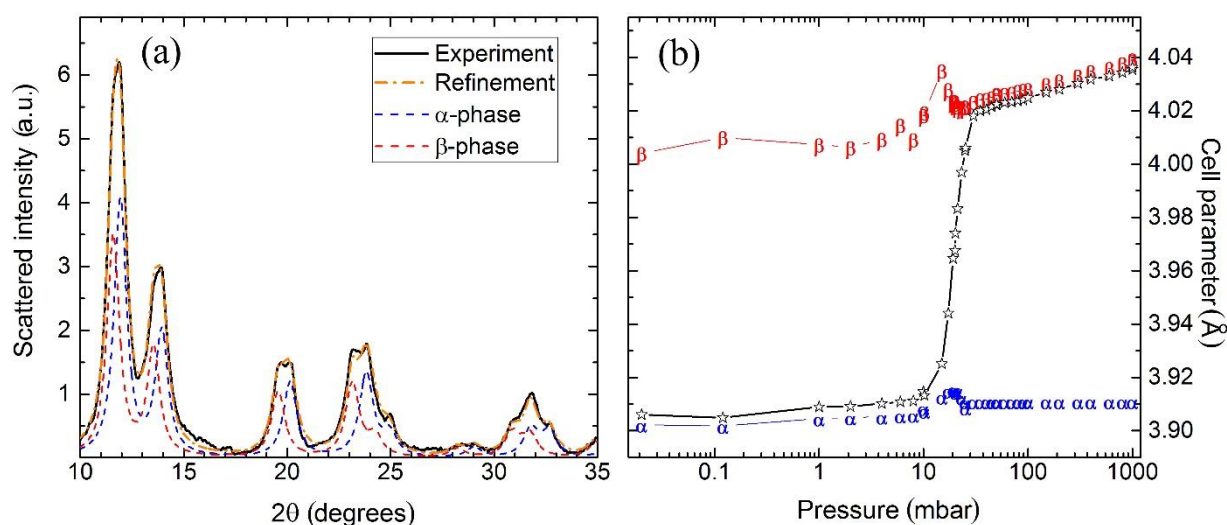


Figure S7. (a) Example of refinement procedure for the XRPD pattern taken at 22 °C under 20 mbar hydrogen pressure. The patterns are shown after the subtraction of the contribution of the carbon support, which was performed during the Rietveld refinement. (b) Results of the Rietveld refinement of the 22 °C isotherm data. Blue and red curves correspond to cell parameters in α - and β - phases respectively. Black curve with stars represent a weight-averaged cell parameter.

Williamson-Hall analysis was performed to analyze size-induced and strain-induced broadening of the XRPD peaks width.^{8,9} Experimental peaks were fitted by a pseudo-Voigt function, which is by definition a linear combination of a Lorentzian function L , and Gaussian function G : $V = \eta L + (1 - \eta)G$. The fitted value of the Lorentzian component η was varied from 95 % at $2\theta = 13^\circ$ to 98 % at $2\theta = 50^\circ$ which indicates the dominant Lorentzian contribution to the integral peak breath. The Williamson-Hall plot is presented in the Figure S8 experimental data corresponding to the angular dependency of the XRPD peak FWHM was fitted by a linear curve, based on the equation: $FWHM \cos(\theta) = \frac{K\lambda}{D} + 4\epsilon \sin(\theta)$, where D is the average particle size, K is the shape factor, and ϵ is a micro-strain due to imperfection and distortion in the crystal structure. The value $K = 0.9$ was taken, considering the spherical shape of the particles. The instrumental broadening was neglected. The obtained values of the particle size and micro-strain are: $D = 2.5$ nm and $\epsilon = 0.003$ %. The former value being in agreement with the TEM study.

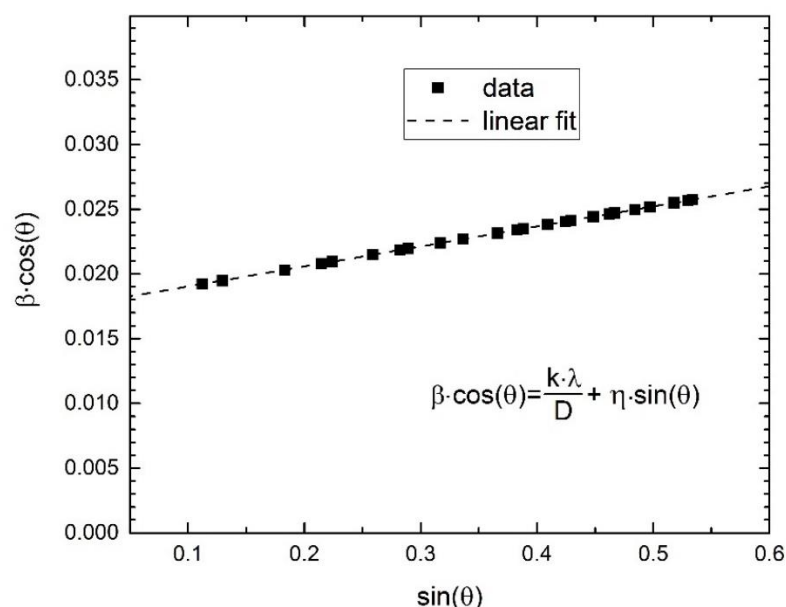


Figure S8. Williamson-Hall analysis for bare palladium nanoparticles at 22 °C.

S4. Volumetric measurements

The pressure-composition isotherms for the Pd/C sample were measured in a temperature range from –13 to 110 °C. The initial data are shown in Figure S9a where the contribution of the carbon support affect the shape of the curves at high pressures. The hydrogen adsorption on carbon, used for supporting the nanoparticles, was measured separately. Figure S9b demonstrates that the amount of hydrogen adsorbed in carbon is linearly proportional to the hydrogen pressure. The final data after subtraction of this contribution, and recalculated from mmol/g to the H/Pd are shown in the Figure S9c. In addition, the pressure-composition isotherms were corrected by the amount of hydrogen adsorbed at low pressure, which correspond to the formation of a hydrogen layer on the surface of the nanoparticles, and not to the formation of the hydride.

The nanometric dimension of the palladium particles resulted in much lower hydrogen uptake of about PdH_{0.4} in β -phase region in respect to PdH_{0.6} reported for bulk palladium.¹⁰⁻¹² This fact indicates a lower number of interstitial sites per gram of material related to the higher surface to volume ratio of the palladium nanoparticles with respect to the bulk.¹² Nevertheless, the lower uptake in the palladium nanoparticle has been also related to the lower critical temperature that can be predicted for palladium nanoparticles with respect to bulk Pd.¹¹⁻¹⁸ The plateau pressure obtained at 22 °C is also close to that reported for the palladium nanoparticles of size < 8 nm, that are known to be characterized by absorption pressures close to that of bulk palladium, differently from nanoparticles with larger sizes.¹¹⁻¹⁸

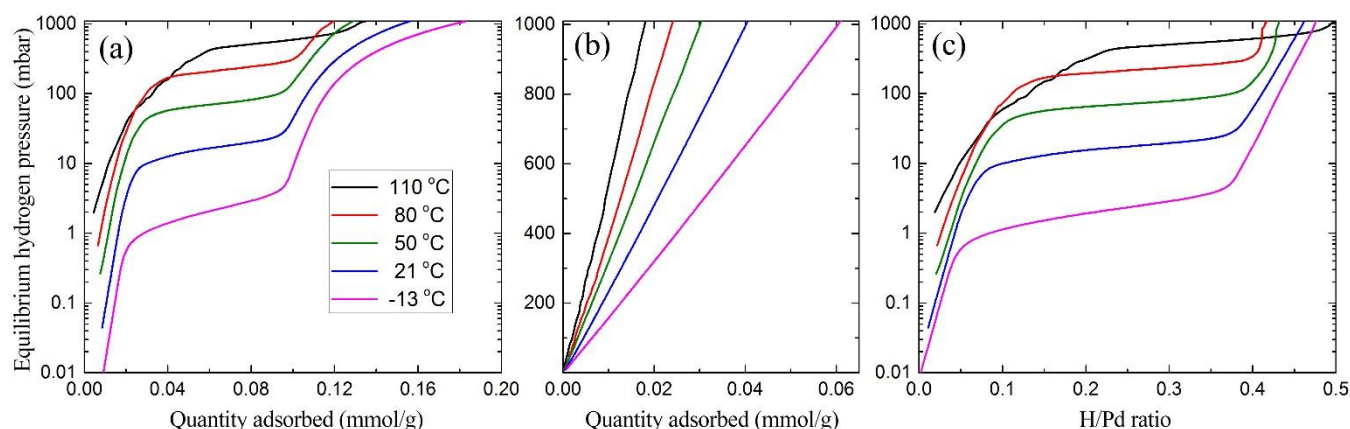


Figure S9. H₂ absorption isotherms for Pd/C sample (a), H₂ absorption in carbon support (b), and PdH pressure-composition isotherms after subtraction of carbon contribution, surface adsorption, and recalculated from mmol/g to H/Pd ratio.

The plateau pressures were chosen in the middle of the plateau region and were used to make a Van 't Hoff plot represented in Figure S10. Van 't Hoff allowed us to compare the thermodynamic of the absorption on this sample with the one obtained for other palladium-based systems.¹⁹ The enthalpic and entropic values obtained for the Pd/C catalyst ($\Delta H = -37 \pm 4 \text{ kJ} \cdot \text{mol}_{\text{H}_2}^{-1}$; $\Delta S = 92 \pm 9 \text{ J} \cdot \text{K}^{-1} \cdot \text{mol}_{\text{H}_2}^{-1}$) were close to those reported for the bulk palladium, as measured by calorimetric measurements ($\Delta H = -37.2 \text{ kJ} \cdot \text{mol}_{\text{H}_2}^{-1}$; $\Delta S = 92.5 \text{ J} \cdot \text{K}^{-1} \cdot \text{mol}_{\text{H}_2}^{-1}$)¹⁶ and for palladium nanoparticles.^{11, 13-18, 20-23} Then, after the determination of the plateau pressures for the pressure-distance isotherms obtained by EXAFS and XRPD (Figure 3 of the main text), we were able to determine the real temperature of the sample inside the capillary in the X-ray measurements. To simulate the pressure-composition isotherms for the same temperatures as EXAFS and XRPD data presented in the Figure 3 of the main text, the following equation was used:

$$\ln(p'(x)) = \frac{\ln(p_1(x)) + \gamma \ln(p_2(x))}{1 + \gamma},$$

where $p_1(x)$ and $p_2(x)$ are experimental isotherms measured at temperatures T_1 and T_2 , $p'(x)$ is a simulated isotherm for the desired temperature T' , and $\gamma = \frac{1/T' - 1/T_1}{1/T_2 - 1/T'}$.

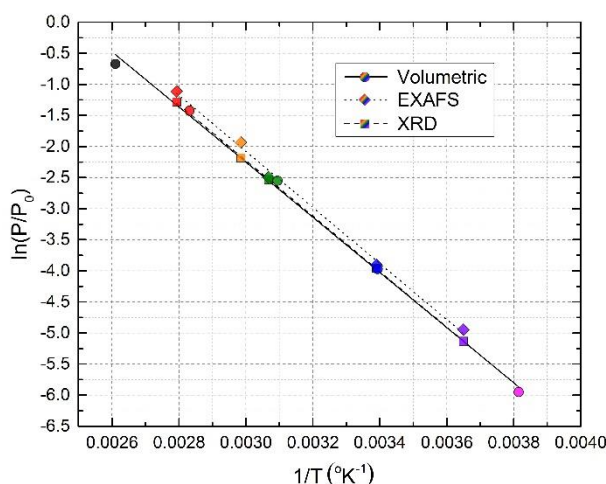


Figure S10. Van 't Hoff plot combining volumetric (solid line, circles), EXAFS (dotted line, diamonds), and XRPD (dashed line, squares) data.

The identical behavior of the Van 't Hoff plots obtained from EXAFS and XRPD indicates that there are no significant changes in enthalpy and entropy for core and shell of the nanoparticles. This result correlates with the fact that there is no clear dependence of the entropic/enthalpic terms on the particle size and shape.^{16, 17, 20} A linear dependence of ΔH on ΔS was also verified in the previous studies, suggesting an enthalpy-entropy compensation effect in H-absorption in Pd based systems, both bulk and nanoparticles.¹⁶

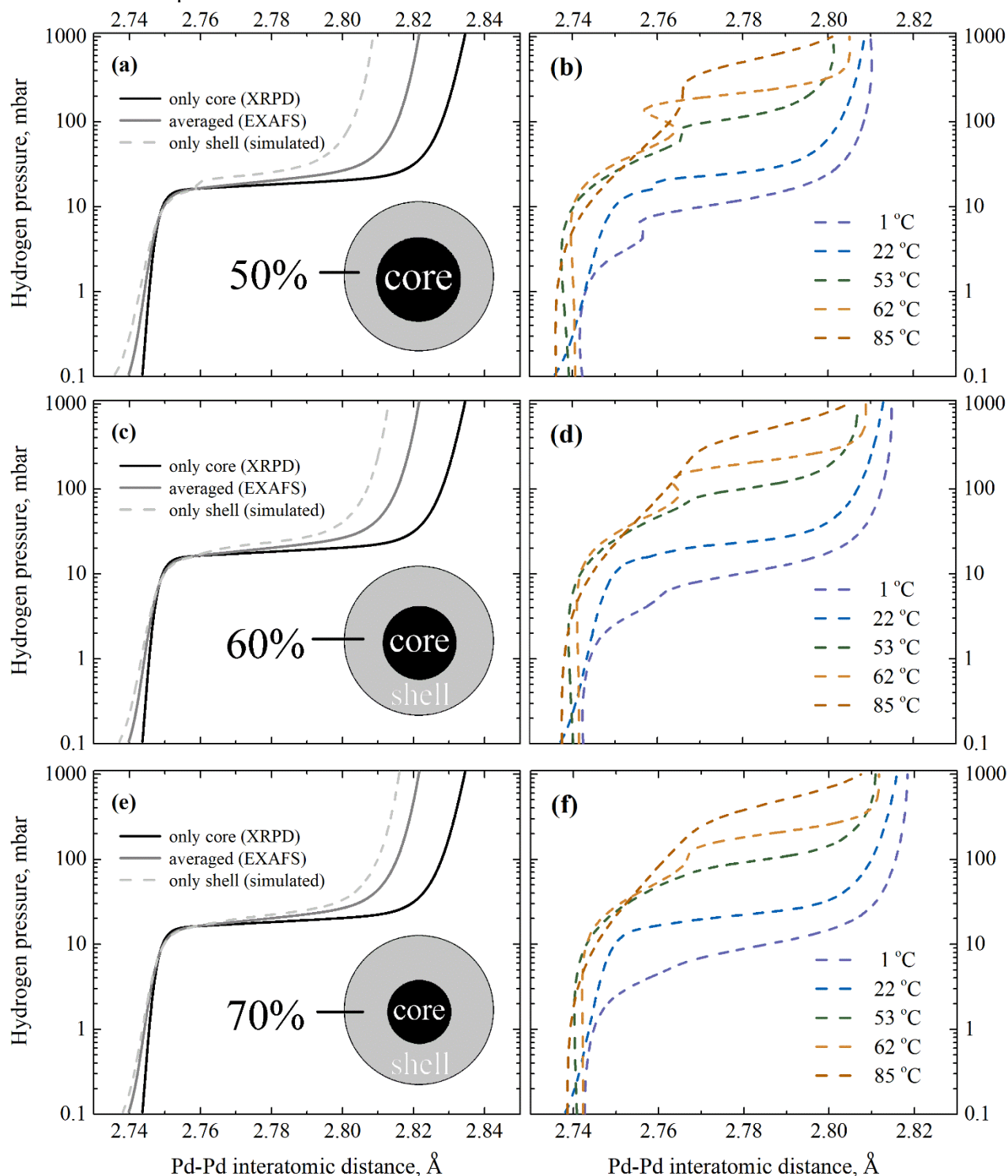


Figure S11. Determination of Pd-Pd distances in the shell of the nanoparticles at 20 °C assuming that the fraction of the shell is equal to 50% (a), 60% (c) and 70% (e). Corresponding isotherms for all temperatures are shown in parts (b), (d) and (f) correspondingly. Parts (c) and (d) are the same as parts (a) and (b) of Figure 5 in the main text.

S5. References.

- (1) Bugaev, A. L.; Guda, A. A.; Lazzarini, A.; Lomachenko, K. A.; Groppo, E.; Pellegrini, R.; Piovano, A.; Emerich, H.; Soldatov, A. V., *et al.* In Situ Formation of Hydrides and Carbides in Palladium Catalyst: when XANES is Better than EXAFS and XRD. *Catal. Today* **2017**, *283*, 119-126.
- (2) Bugaev, A. L.; Guda, A. A.; Lomachenko, K. A.; Srabionyan, V. V.; Bugaev, L. A.; Soldatov, A. V.; Lamberti, C.; Dmitriev, V. P.; van Bokhoven, J. A. Temperature- and pressure-Dependent Hydrogen Concentration in Supported PdH_x Nanoparticles by Pd K-edge X-ray Absorption Spectroscopy. *J. Phys. Chem. C* **2014**, *118*, 10416-10423.
- (3) Bugaev, A. L.; Srabionyan, V. V.; Soldatov, A. V.; Bugaev, L. A.; van Bokhoven, J. A. The Role of Hydrogen in Formation of Pd XANES in Pd-Nanoparticles. *J. Phys. Conf. Ser.* **2013**, *430*, Art. n. 012028.
- (4) Tew, M. W.; Miller, J. T.; van Bokhoven, J. A. Particle Size Effect of Hydride Formation and Surface Hydrogen Adsorption of Nanosized Palladium Catalysts: L₃ Edge vs. K Edge X-ray absorption Spectroscopy. *J. Phys. Chem. C* **2009**, *113*, 15140-15147.
- (5) Ravel, B.; Newville, M. ATHENA, ARTEMIS, HEPHAESTUS: Data Analysis for X-Ray Absorption Spectroscopy using IFEFFIT. *J. Synchrotron Radiat.* **2005**, *12*, 537-541.
- (6) Srabionyan, V. V.; Bugaev, A. L.; Pryadchenko, V. V.; Avakyan, L. A.; van Bokhoven, J. A.; Bugaev, L. A. EXAFS Study of Size Dependence of Atomic Structure in Palladium Nanoparticles. *J. Phys. Chem. Solids* **2014**, *75*, 470-476.
- (7) Petříček, V.; Dušek, M.; Palatinus, L. Crystallographic Computing System JANA2006: General Features. *Z. Kristallog.* **2014**, *229*, 345-352.
- (8) Suryanarayana, C.; Norton, M. G., *X-Ray Diffraction: a Practical Approach*. Springer Science & Business Media: New York, 1998.
- (9) Williamson, G. K.; Hall, W. H. X-ray Line Broadening from Filled Aluminium And Wolfram. *Acta Metall.* **1953**, *1*, 22-31.
- (10) Flanagan, T. B.; Oates, W. A. The Palladium-Hydrogen System. *Annu. Rev. Mater. Sci.* **1991**, *21*, 269-304.
- (11) Griessen, R.; Strohheldt, N.; Griessen, H. Thermodynamics of the hybrid Interaction of Hydrogen with Palladium Nanoparticles. *Nat. Mater.* **2016**, *15*, 311-317.
- (12) Zuttel, A.; Nutzenadel, C.; Schmid, G.; Emmenegger, C.; Sudan, P.; Schlapbach, L. Thermodynamic aspects of the interaction of hydrogen with Pd clusters. *Appl. Surf. Sci.* **2000**, *162*, 571-575.
- (13) Baldi, A.; Narayan, T. C.; Koh, A. L.; Dionne, J. A. In situ Detection of Hydrogen-Induced Phase Transitions in Individual Palladium Nanocrystals. *Nat. Mater.* **2014**, *13*, 1143-1148.
- (14) Bardhan, R.; Hedges, L. O.; Pint, C. L.; Javey, A.; Whitlam, S.; Urban, J. J. Uncovering the Intrinsic Size Dependence of Hydriding Phase Transformations In Nanocrystals. *Nat. Mater.* **2013**, *12*, 905-912.
- (15) Sachs, C.; Pundt, A.; Kirchheim, R.; Winter, M.; Reetz, M. T.; Fritsch, D. Solubility of hydrogen in Single-Sized Palladium Clusters. *Phys. Rev. B* **2001**, *64*, Art. n. 075408.
- (16) Syrenova, S.; Wadell, C.; Nugroho, F. A. A.; Gschneidner, T. A.; Fernandez, Y. A. D.; Nalin, G.; Switlik, D.; Westerlund, F.; Antosiewicz, T. J., *et al.* Hydride Formation Thermodynamics and Hysteresis in Individual Pd Nanocrystals with Different Size and Shape. *Nat. Mater.* **2015**, *14*, 1236-1244.
- (17) Wadell, C.; Pingel, T.; Olsson, E.; Zoric, I.; Zhdanov, V. P.; Langhammer, C. Thermodynamics of Hydride Formation and Decomposition in Supported sub-10 nm Pd Nanoparticles of Different Sizes. *Chem. Phys. Lett.* **2014**, *603*, 75-81.
- (18) Yamauchi, M.; Ikeda, R.; Kitagawa, H.; Takata, M. Nanosize Effects on Hydrogen Storage in Palladium. *J. Phys. Chem. C* **2008**, *112*, 3294-3299.

- (19) Griessen, R.; Riesterer, T., Heat of formation models. In *Hydrogen in Intermetallic Compounds I: Electronic, Thermodynamic, and Crystallographic Properties, Preparation*, Schlapbach, L., Ed. Springer Berlin Heidelberg: Berlin, Heidelberg, 1988; Vol. 63, pp 219-284.
- (20) Berube, V.; Radtke, G.; Dresselhaus, M.; Chen, G. Size Effects on the Hydrogen Storage Properties of Nanostructured Metal Hydrides: a Review. *Int. J. Energy Res.* **2007**, *31*, 637-663.
- (21) Fischer, F. D.; Waitz, T.; Vollath, D.; Simha, N. K. On the Role of Surface Energy and Surface Stress in Phase-Transforming Nanoparticles. *Prog. Mater. Sci.* **2008**, *53*, 481-527.
- (22) Ingham, B.; Toney, M. F.; Hendy, S. C.; Cox, T.; Fong, D. D.; Eastman, J. A.; Fuoss, P. H.; Stevens, K. J.; Lassesson, A., *et al.* Particle Size Effect of Hydrogen-Induced Lattice Expansion of Palladium Nanoclusters. *Phys. Rev. B* **2008**, 78.
- (23) Langhammer, C.; Zhdanov, V. P.; Zoric, I.; Kasemo, B. Size-Dependent Hysteresis in the Formation and Decomposition of Hydride in Metal Nanoparticles. *Chem. Phys. Lett.* **2010**, *488*, 62-66.